

A Comprehensive Vehicle Stability Assessment System Based on Enabling Tire Force Estimation

Xiaolin Ding , Zhenpo Wang , *Member, IEEE*, Lei Zhang , *Member, IEEE*, and Jizheng Liu 

Abstract—This paper presents an enabling comprehensive vehicle stability assessment system covering vehicle longitudinal, yaw and roll stability. First, the longitudinal, lateral and vertical tire forces are separately estimated using the strong tracking unscented Kalman filter and the conventional Kalman filter based on low-cost on-board sensors. Then, a comprehensive vehicle longitudinal, yaw and roll stability space is established by utilizing the normalized tire friction ellipse and the Load Transfer Ratio value. Finally, the vehicle stability is determined and predicted based on current driver's inputs. The hardware-in-loop experimental results show that the proposed vehicle stability assessment system can accurately estimate the longitudinal, lateral and vertical tire forces with the normalized root mean square errors of 1.87%, 1.07% and 1.43%, and exhibits satisfying performance for vehicle longitudinal, yaw and roll stability evaluation and prediction. This bears significance for the efficient functioning of active control systems to improve vehicle safety under critical driving conditions.

Index Terms—Active safety control, tire force estimation, vehicle stability assessment, vehicle stability prediction, strong tracking unscented Kalman filter.

I. INTRODUCTION

VEHICLE stability control systems (VSCs) are pivotal to enhance vehicle dynamics stability especially under critical driving conditions [1]–[3]. These mainly include Acceleration Slip Regulation (ASR) [4], Torque Vectoring and Anti-Roll System (ARS) [5]. Comprehensive and accurate vehicle dynamics stability assessment is a requisite for appropriately activating these safety control systems. In real vehicular operations, vehicle dynamics instability could originate from longitudinal, yaw and roll motions and is subjective to their coupling effects. Substantial efforts have been directed to achieving real-time vehicle stability assessment, which can be roughly categorized into three categories, i.e., longitudinal, yaw and roll stability assessments.

Vehicle longitudinal stability assessment is fundamental for the timely intervention of the Anti-lock Braking System (ABS) and ASR for vehicle longitudinal stability control. The threshold

method is widely adopted based on tire slip ratio [6] or wheel angular acceleration [7] for activating vehicle longitudinal control. This has been maturely implemented in commercialized ABS and ASR. For yaw stability evaluation, the reported methods can be generally assorted into two groups, i.e., model- and phase plane-based methods. The model-based method utilizes the deviation between the actual and the desired yaw rate or other yaw-related states as the triggering condition of yaw stability control [8]. But these methods need to set proper thresholds in advance and exhibit poor adaptiveness to varying driving conditions. For the phase plane-based method, vehicle sideslip angle, yaw rate and lateral velocity are often used to form a two-dimensional phase plane by employing any two of the three entities, in which a certain region is appropriated as the stability region [9]–[11]. But the boundaries of the designated stability region are variable depending on vehicle speed, front-wheel steering angle and road friction conditions [12]. This volatility may destabilize the underlying active safety controller under complex driving scenarios [13]. To tackle this issue, some studies have been carried out by incorporating the vehicle dynamics constraint [14] or by introducing the impacts of other vehicle motions [15].

For roll stability evaluation, several roll stability indexes have been used. These indexes mainly include characteristic state-, energy analysis- and force analysis-based methods [16], [17]. The characteristic state-based method employs roll motion-related parameters such as lateral acceleration, roll rate and roll angle for evaluating vehicle roll stability [18]. This method has no use of accurate vehicle or suspension models and is straightforward and easy to implement [19], [20]. But it cannot depict vehicle roll dynamics and its efficacy is highly reliant on the rule of thumb and massive field tests. In contrast, the energy analysis-based method employs vehicle kinetics, potential and dissipation energies for roll stability assessment [21]. But challenges remain in the accurate acquisition of key vehicle states and parameters required for calculating the energy flow under varied driving conditions. The force analysis-based method utilizes vehicle dynamics characteristics to assess vehicle roll stability. The Zero-Moment Point (ZMP) and the Lateral Load Transfer Ratio (LTR) approach exemplify this kind of method. Lapamong et al. [22] assessed vehicle roll stability by comparing the lateral position of ZMP with the wheelbase. The LTR method employs the difference between the left and the right vertical tire load to quantitatively assess vehicle rollover propensity [16], [17]. Some studies have tried to combine the time-to-rollover scheme with the LTR or ZMP for vehicle roll stability assessment [23].

Manuscript received 7 January 2022; revised 21 April 2022 and 6 June 2022; accepted 14 July 2022. Date of publication 22 July 2022; date of current version 14 November 2022. This work was supported by Beijing Municipal Science and Technology Commission through Beijing Nova Program under Grant Z201100006820007. The review of this article was coordinated by Prof. Yan Chen. (*Corresponding author: Lei Zhang.*)

The authors are with the Collaborative Innovation Center for Electric Vehicles in Beijing, Beijing Institute of Technology, Beijing 100081, China and also with the National Engineering Research Center of Electric Vehicles, Beijing Institute of Technology, Beijing 100081, China (e-mail: lei_zhang@bit.edu.cn).

Digital Object Identifier 10.1109/TVT.2022.3193139

Previous studies have presented various methods for vehicle stability assessment. The longitudinal stability assessment compares the tire slip ratio with pre-set thresholds for longitudinal stability evaluation. This method is straightforward and easy to understand, but cannot demonstrate the coupling relationship between the longitudinal and the lateral stability. With the constraint of tire-road friction, the longitudinal instability often leads to small margins of lateral stability. For yaw stability assessment, the commonly-used phase plane-based method requires a large number of field tests to obtain respective stability regions under different vehicle velocities, steering angles and road adhesion conditions. This significantly increases the testing workload and cannot ensure the robustness to varying driving conditions. The vehicle rollover stability assessment method only evaluates a single roll state, and cannot accurately describe the coupling relationship between vehicle lateral and roll motions. In a nutshell, a comprehensive vehicle stability assessment system that can simultaneously evaluate vehicle longitudinal, yaw and roll stability is still absent in the literature. However, efficient and comprehensive vehicle stability assessment bears enormous significance for triggering safety control systems and for synthesizing specific control targets of chassis coordinated control.

Vehicle stability state is essentially a comprehensive reflection of four tires' force states, and vehicle longitudinal, lateral and roll dynamics are strongly coupled with the longitudinal, lateral and vertical tire forces at each wheel [24]. Thus, accurate acquisition of tire forces in real-time can be straightforwardly utilized to evaluate overall vehicle stability. The reported tire force estimation methods in the literature can be categorized into the observer- and sensor-based methods [25]. The sensor-based method utilizes the tire tread sensors [26] or load sensing bearing [27] to directly measure the deflection of tread elements or hub bearing strain for tire force estimation. However, these tire force measurement sensors are expensive and commercially prohibitive for being used in mass-production vehicles [28]. The observer-based method usually integrates vehicle dynamics and tire models with specialized state observers for tire force estimation [29], [30]. Nevertheless, the tire model-based estimation methods, like the Dugoff-based [31], LuGre-based [12], Magic formula-based [32], etc., need to tune model parameters under different tire loads, and the ubiquitous noises with tire sideslip angle and slip ratio also seriously compromise the estimation accuracy. Therefore, developing a model-free estimation scheme is a viable way to improve the accuracy and robustness of estimation.

To realize coordinated control of chassis subsystems, this paper proposes an enabling vehicle stability assessment system based on tire force estimation by utilizing low-cost on-board sensors. First, the longitudinal, lateral and vertical tire forces are estimated using the Strong Tracking Unscented Kalman filter (STUKF) based on low-cost on-board sensors. Second, a spatial vehicle stability assessment system is synthesized utilizing the normalized tire friction ellipse and the LTR value. Finally, the present and futuristic vehicle stability can be determined and predicted based on current vehicle states and driver's inputs. The Hardware-in-Loop (HIL) test results show that the proposed vehicle stability assessment system can accurately estimate the

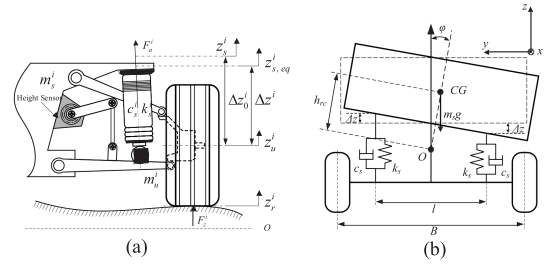


Fig. 1. Vehicle roll dynamics models. (a) is a quarter suspension model, (b) is the schematic of vehicle roll dynamics.

longitudinal, lateral and vertical tire forces, and exhibits excellent performance for vehicle stability evaluation and prediction. The major contributions of this study to the related literature can be summarized in the following aspects.

- Aiming to improve the robustness and accuracy of tire forces estimation, a longitudinal, lateral and vertical tire force estimation scheme is developed based on low-cost on-board sensors without using any tire model.
- Based on estimated tire forces, a spatial vehicle stability assessment system is synthesized utilizing the normalized tire friction ellipse and the LTR value.
- The proposed comprehensive vehicle stability assessment system can simultaneously evaluate the vehicle longitudinal, yaw and roll stability in real-time without requiring labor-intensive field tests.

The remainder of this paper is arranged as follows: Section II introduces the estimation-oriented system models. Section III elaborates on the proposed vehicle stability assessment and prediction system. Section IV provides the HIL experimental verification, followed by the key conclusions summarized in Section V.

II. ESTIMATION-ORIENTED SYSTEM MODELLING

For accurately assessing and predicting the tire and vehicle motion states, the roll, lateral and longitudinal vehicle models are established, respectively.

A. Roll Dynamics Model

A quarter active suspension system is illustrated in Fig. 1(a). Ignoring the change of the effective tire rolling radius, the vehicle roll dynamics model is given by

$$k_s^i (z_s^i - z_u^i - \Delta z_0^i) + c_s^i (\dot{z}_s^i - \dot{z}_u^i) + F_a^i - m_s^i \ddot{z}_s^i - m_s^i g = 0 \quad (1)$$

where z_s^i and z_u^i represent the vertical displacements of the sprung and the unsprung mass with the superscript $i \in [L1, R1, L2, R2]$ representing front-left, front-right, rear-left, and rear-right, respectively; F_a^i is the actuator force of active suspension; m_s^i denotes the distributed sprung mass on each wheel; k_s^i and c_s^i are the stiffness and damping of each suspension, which can be obtained from the active suspension controller; g is the gravity acceleration; Δz_0^i is the height of suspension without deformation.

For the active suspension, the combined vertical displacement of the sprung and unsprung masses can be measured by a suspension height sensor. Equation (1) can be further deduced

as

$$k_s^i (\Delta z^i - \Delta z_0^i) + c_s^i \Delta \dot{z}^i + F_a^i - m_s^i \ddot{z}_s^i - m_s^i g = 0 \quad (2)$$

where Δz^i is the combined vertical displacement of the sprung and unsprung masses measured by the suspension height sensor.

Tire vertical force F_z^i consists of the static and dynamic loads. The static tire force is caused by the weights of the unsprung mass m_u^i and the sprung mass m_s^i distributed at each corner while the dynamic load corresponds to the load transfer caused by the lateral and longitudinal vehicle motions. Thus, the tire vertical force $F_z^i(z_u^i, z_r^i)$ can be deduced by

$$F_z^i(z_u^i, z_r^i) - k_s^i (\Delta z^i - \Delta z_0^i) - c_s^i \Delta \dot{z}^i - F_a^i - m_u^i g - m_u^i \ddot{z}_u^i - F_{cam}^i (\Delta z^i, \Delta \dot{z}^i) = 0 \quad (3)$$

where $F_{cam}^i(\Delta z^i, \Delta \dot{z}^i)$ denotes the effects of the wheel alignment parameters on the vertical force; z_r^i is the random road excitation. To accurately predict the vertical tire force, a vehicle roll dynamics model with an active suspension system is set up as shown in Fig. 1(b). The vehicle coordinate system is defined as follows: x -axis denotes the vehicle longitudinal axis and is positive in the vehicle forward direction; y -axis represents the vehicle lateral axis and is positive in the left-hand direction; z -axis is perpendicular to the x - y plane and is positive in the upward direction. To simplify the vehicle roll dynamics model, the effects of the roll angle of the unsprung mass and of the side wind are neglected, and thus the equations of roll motion can be formulated as

$$c_\varphi \dot{\varphi} + k_\varphi \varphi = m_s a_y h_{rc} \cos \varphi + m_s g h_{rc} \sin \varphi - I_x \ddot{\varphi} \quad (4)$$

where φ , m_s and a_y are the roll angle, sprung mass and lateral acceleration; h_{rc} is the vertical distance from the center of gravity (CG) to the roll center; I_x represents the moment of inertia of the sprung mass around the x -axis at the CG. The rolling angular stiffness k_φ and the damping coefficient c_φ can be calculated by [43]

$$k_\varphi = \frac{l^2}{4} \sum k_s^i, \quad c_\varphi = \frac{l^2}{4} \sum c_s^i \quad (5)$$

where l is the distance between the left and the right suspension mounting position on the same axle, assuming that the mounting positions of the front and rear suspensions are the same.

Due to the small roll angle with $\sin \varphi \approx \varphi$ and $\cos \varphi \approx 1$, Equation (5) can be simplified as

$$I_x \ddot{\varphi} = m_s a_y h_{rc} + m_s g h_{rc} \varphi - k_\varphi \varphi - c_\varphi \dot{\varphi} \quad (6)$$

The compression of the suspension system on each wheel leads to vehicle roll motion. Thus, the relationship between the vehicle roll state and the kinematics of each suspension can be expressed as

$$\Delta z_s^i = \Upsilon^i(\varphi), \quad \Delta z_u^i = \Upsilon^i(\dot{\varphi}) \quad (7)$$

where the kinematic function Υ^i can be fitted offline.

B. Lateral Vehicle Model

For accurately estimating the lateral tire force in the linear and nonlinear regions, a simplified four-wheel lateral vehicle

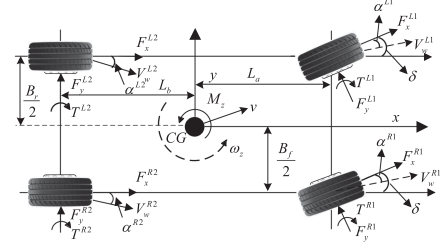


Fig. 2. The 3-DOF vehicle model.

model is built as shown in Fig. 2. The dynamic relationship can be given by

$$\begin{aligned} m a_y &= (F_x^{L1} + F_x^{R1}) \sin \delta + (F_y^{L1} + F_y^{R1}) \cos \delta + (F_y^{L2} + F_y^{R2}) \\ I_z \dot{\omega}_z &= L_a ((F_x^{L1} + F_x^{R1}) \sin \delta + (F_y^{L1} + F_y^{R1}) \cos \delta) \\ &\quad - L_b (F_y^{L2} + F_y^{R2}) + \frac{B_f}{2} ((F_x^{L1} - F_x^{R1}) \cos \delta \\ &\quad + (F_y^{L1} - F_y^{R1}) \sin \delta) + \frac{B_r}{2} (F_x^{L2} - F_x^{R2}) \end{aligned} \quad (8)$$

where m is the vehicle mass; L_a and L_b are the horizontal distances from the front and rear axles to the CG; F_x^i and F_y^i represent the longitudinal and lateral tire forces; δ , $\dot{\omega}_z$ and I_z are the front-wheel steering angle, yaw acceleration and moment of inertia around the z -axis; B_r and B_f are the front and rear tread widths.

According to Ref. [33], each individual lateral tire force complies to the vertical force distribution, which can be given by

$$\begin{aligned} F_y^{L1,R1} &= \frac{F_z^{L1,R1}}{g} (a_y + \dot{\omega}_z L_a) \\ F_y^{L2,R2} &= \frac{F_z^{L2,R2}}{g} (a_y - \dot{\omega}_z L_b) \end{aligned} \quad (9)$$

where F_z^i is the vertical tire force.

In order to describe the relationship between the vehicle lateral dynamics and the front-wheel steering angle, a linearized lateral tire model is established as

$$F_y^j = C_\alpha^j \alpha^j \quad (10)$$

where C_α^j and α^j are the cornering stiffness and tire slip angle of each axle. The superscript $j \in [f, r]$ represents the cornering stiffness of the front axle and of the rear axle. For the front and rear wheels, the tire side slip angle can be calculated by

$$\alpha^f = \beta + \frac{L_a \omega_z}{v_x} - \delta, \quad \alpha^r = \beta - \frac{L_b \omega_z}{v_x} \quad (11)$$

where β and v_x are the vehicle sideslip angle and vehicle longitudinal velocity.

Ignoring the longitudinal tire force, Equation (8) can be simplified as

$$\begin{aligned} ma_y &= C_\alpha^f \left(\beta + \frac{L_a \omega_z}{v_x} - \delta \right) + C_\alpha^r \left(\beta - \frac{L_b \omega_z}{v_x} \right) \\ I_z \dot{\omega}_z &= L_a C_\alpha^f \left(\beta + \frac{L_a \omega_z}{v_x} - \delta \right) - L_b C_\alpha^r \left(\beta - \frac{L_b \omega_z}{v_x} \right) \end{aligned} \quad (12)$$

C. Longitudinal Vehicle Model

A single-wheel model is used to describe the dynamics of each wheel, and the equation of motion is given by

$$J_\omega \dot{\omega}^i = T_d^i - T_b^i - F_x^i R_e - F_f^i R_e \quad (13)$$

where T_d^i , T_b^i , F_f^i , ω^i , R_e and J_ω represent the driving torque, braking torque, rolling resistance, angular speed, effective radius and moment of inertia of the wheel, respectively.

The tire slip ratio is defined as

$$\lambda^i = \frac{\omega^i R_e - v_x}{v_x} \quad (14)$$

To describe the longitudinal vehicle dynamics response, a longitudinal vehicle model is given by

$$\begin{aligned} ma_x &= \sum F_x^i - \sum F_f^i - F_w - F_i \\ \sum F_x^i &= (F_x^{L1} + F_x^{R1}) \cos \delta - (F_y^{L1} + F_y^{R1}) \sin \delta \\ &\quad + (F_x^{L2} + F_x^{R2}) \end{aligned} \quad (15)$$

where $\sum F_x^i$, F_w , $\sum F_f^i$, and F_i represent the total longitudinal driving force, air resistance, rolling resistance and grade resistance, which can be calculated by

$$\begin{cases} \sum F_f^i = mgf \\ F_w = \frac{1}{2} \rho C_D A v_x^2 \\ F_i = mg \sin \theta \end{cases} \quad (16)$$

where C_D is the aerodynamic resistance coefficient; A is the windward area; ρ is the air density; f is the rolling resistance coefficient and is treated as a constant here [35]; θ is the road gradient. It is worth noted that the aerodynamic and rolling resistances can be obtained through field vehicle tests, while the grade resistance can be reliably estimated [34].

III. TIRE FORCE-BASED VEHICLE STABILITY ASSESSMENT AND PREDICTION

The vehicle stability refers to that a vehicle can keep itself stable or quickly restore to the stable driving state after disturbed by external factors, such as dramatic driver's inputs, sudden road friction change, etc. Generally, it is the ability that can prevent the vehicle from wheel slip, drifting or rollover under a diverse range of driving conditions.

Vehicle stability usually focuses on three aspects, i.e., the longitudinal, yaw and roll stability. The longitudinal stability refers to the ability to prevent wheels from slipping or locking during vehicle longitudinal motion. Emergency acceleration and braking are two typical scenarios raising longitudinal stability issues. In wheel slipping or locking, the longitudinal tire

force reaches saturation and shows a gradual decline with the increasing slip ratio. The vehicle yaw stability is to ensure that the vehicle yaw motion can accommodate the driver's steering intentions to avoid vehicle understeer or oversteer (spin) under cornering conditions. When the vehicle becomes unstable in yaw motion, the yaw rate and sideslip angle often exceed their respective limits, and the lateral tire force exhibits a nonlinear relationship with the steering angle. The vehicle roll stability means the anti-roll ability to prevent the inner wheels from lifting off the ground under sharp steering maneuvers. In general, vehicle stability is essentially a comprehensive indication of four tires' force states.

The flowchart of the proposed tire force-based vehicle stability assessment and prediction system is given in Fig. 3. The low-cost on-board sensors including the suspension ride height sensor, IMU sensor, in-wheel motors, steering angle encoder and pedal position sensors (acceleration and brake signal states, etc.) are simultaneously used to obtain the suspension compression, vehicle inertia states and front-wheel steering angle, respectively. In addition to the motor output torques and rotational speeds provided by each in-wheel motor, these signals are used as the inputs to the tire force estimation and prediction module. More details about the used low-cost sensors are given in Table I. In the tire force estimation and prediction module, three types of tire force estimators are developed to estimate the longitudinal, lateral and vertical tire forces of each tire using the STUKF estimator. Without using complex tire models such as the Dugoff and the Magic formula tire model whose parameters are difficult to obtain in real-time, the robust and accuracy of tire force estimation can be improved. In order to develop a comprehensive vehicle stability assessment system for simultaneous longitudinal, yaw and roll stability evaluation, the estimated longitudinal- and lateral tire forces of each tire are normalized to form a tire friction ellipse, which can be divided into four stability regions according to the planar motion state, and the four vertical tire forces are used to calculate the LTR value. Based on the tire friction ellipse and the LTR value, a comprehensive vehicle stability space can be established to evaluate vehicle longitudinal, lateral and roll stability.

A. Strong Tracking Unscented Kalman Filter

Compared with the traditional UKF, the STUKF has better performance in tire dynamics tracking and convergence speed. It is worth noted that the STUKF proposed by [37] is employed to tackle the modelling uncertainty and external disturbances in tire force estimation. Consider a discrete time-varying nonlinear stochastic control system as

$$\begin{cases} \mathbf{x}_k = f(\mathbf{x}_{k-1}, \mathbf{u}_{k-1}) + \mathbf{w}_{k-1} \\ \mathbf{z}_k = h(\mathbf{x}_k) + \mathbf{v}_k \end{cases} \quad (17)$$

where $\mathbf{x}_k \in \mathbb{R}^n$ is the state vector; $\mathbf{u}_k \in \mathbb{R}^p$ is the control input; $\mathbf{z}_k \in \mathbb{R}^m$ is the measurement; $\mathbf{w}_{k-1} \in \mathbb{R}^r$ and $\mathbf{v}_k \in \mathbb{R}^m$ are assumed to be white noises with respective covariance matrices of $\mathbf{Q} \in \mathbb{R}^{p \times p}$ and $\mathbf{R} \in \mathbb{R}^{m \times m}$; $f(\cdot)$ and $h(\cdot)$ are the state evolution and measurement functions.

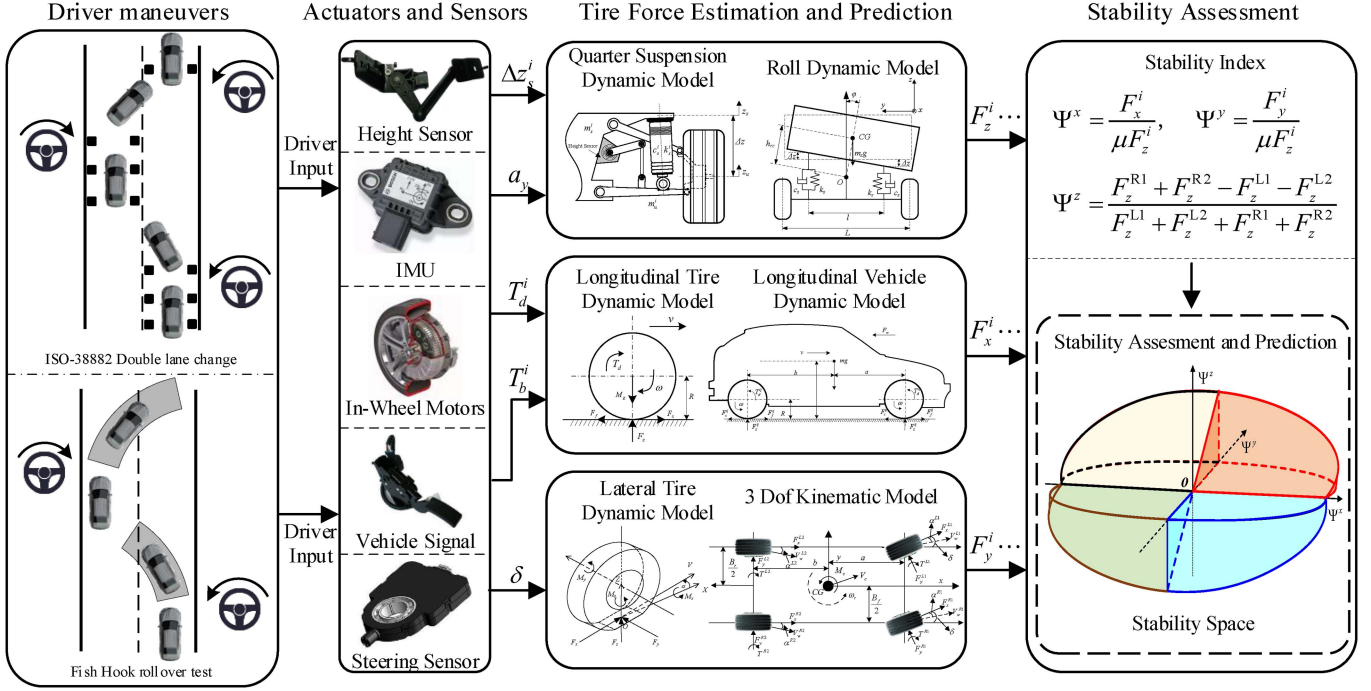


Fig. 3. The flowchart of the proposed tire force-based vehicle stability assessment and prediction system.

TABLE I
SPECIFICATIONS OF THE USED LOW-COST SENSORS

Type	Output Range	Accuracy (RMS)	Application
Inertia Measurement Unit (Continental SC07.1)	Yaw Acc: $[-22.75 \pi, 22.75 \pi]$ Lateral Acc: $[-4.2 \text{ g}, 4.2 \text{ g}]$ Roll Rate: $[-6 \pi, 6 \pi]$ Longi Acc: $[-4.2 \text{ g}, 4.2 \text{ g}]$	Yaw Acc: $7.0\text{e-}4 \text{ rad}\cdot\text{s}^{-2}$ Lateral Acc: 0.004 g Roll Rate: $5.6\text{e-}4 \text{ rad}\cdot\text{s}^{-1}$ Longi Acc: 0.004 g	Measurement of lateral tire estimator Measurement of lateral tire estimator Vertical tire force prediction \
Suspension Ride Height Sensor (Continental chassis position sensor)	Angle: $[0, 0.5 \pi]$ or Position: $[0, 100\text{mm}]$	Angle: $1.22\text{e-}4 \text{ rad}$ or Position: 0.0154 mm	Measurement of lateral tire force estimator
In-wheel motor	Torque: $[-800, 800] \text{ Nm}$ Speed: $[0, 1600] \text{ rpm}$	\	Input of longitudinal tire force estimator Measurement of longitudinal tire force estimator
Steering Wheel Angle Sensor (Bosch ESP Sensor)	Angle: $[-6 \pi, 6 \pi]$ Angle Speed: $[0, 5.67\pi]$	Angle: $5.6\text{e-}4 \text{ rad}$ Angle Speed: $0.070 \text{ rad}\cdot\text{s}^{-1}$	Input of lateral tire force estimator Lateral tire force prediction

(1) Initiation

$$\hat{\mathbf{x}}_0 = E(\mathbf{x}_0)$$

$$\mathbf{P}_0 = E[(\mathbf{x}_0 - \hat{\mathbf{x}}_0)(\mathbf{x}_0 - \hat{\mathbf{x}}_0)^T] \quad (18)$$

(2) Unscented transformation
Calculate the sigma points by

$$\begin{cases} \chi_{0,k-1} = \hat{\mathbf{x}}_{k-1}, i = 0 \\ \chi_{i,k-1} = \hat{\mathbf{x}}_{k-1} + \left(\sqrt{(n+\nu) \mathbf{P}_{k-1}} \right)_i, i = 1, 2, \dots, n \\ \chi_{i,k-1} = \hat{\mathbf{x}}_{k-1} - \left(\sqrt{(n+\nu) \mathbf{P}_{k-1}} \right)_i, i = n+1, \dots, 2n \end{cases} \quad (19)$$

where $\nu = e^2(\ell + \kappa) - \ell$, $10^{-4} \leq e \leq 1$, $\kappa = 3 - \ell$, ℓ is the number of variables. The sigma matrix can be expressed as

$$\chi_{i,k-1} = \left[\hat{\mathbf{x}}_{k-1}, \hat{\mathbf{x}}_{k-1} + \sqrt{(n+\nu) \mathbf{P}_{k-1}}, \hat{\mathbf{x}}_{k-1} - \sqrt{(n+\nu) \mathbf{P}_{k-1}} \right] \quad (20)$$

(3) Time update

The predicted state is given by

$$\chi_{i,k|k-1}^- = f(\chi_{i,k-1}, \mathbf{u}_{k-1}) + \mathbf{w}_{k-1} \quad (21)$$

The predicted mean and covariance are computed as

$$\hat{\mathbf{x}}_{k|k-1}^- = \sum_{i=0}^{2n} \omega_i^m \chi_{i,k|k-1}^-$$

$$\mathbf{P}'_{k|k-1} = \sum_{i=0}^{2n} \omega_i^c \left[\chi_{i,k|k-1}^- - \hat{\mathbf{x}}_{k|k-1}^- \right] \left[\chi_{i,k|k-1}^- - \hat{\mathbf{x}}_{k|k-1}^- \right]^T + \mathbf{Q}_{k-1} \quad (22)$$

where the process noise \mathbf{Q}_{k-1} is initially determined based on the input signals and modelling accuracy, and can be adjusted according to real-time estimation performance; ω_i^m and ω_i^c are

the weighting factors, which can be calculated by

$$\begin{aligned}\omega_0^m &= \frac{\nu}{n + \nu} \\ \omega_0^c &= \frac{\nu}{n + \nu} + (1 - e^2 + \beta) \\ \omega_i^m &= \omega_i^c = \frac{1}{2(n + \nu)}, i = 1, 2, \dots, 2n\end{aligned}\quad (23)$$

(4) Measurement update

The predicted observation can be deduced as

$$\mathbf{z}_{i,k|k-1}^- = h(\mathbf{x}_{i,k|k-1}^-) \quad (24)$$

The predicted observation mean and covariance are calculated by

$$\begin{aligned}\hat{\mathbf{z}}_{k|k-1} &= \sum_{i=0}^{2n} \omega_i^m \mathbf{z}_{k|k-1}^- \\ \mathbf{P}'_{zz,k} &= \sum_{i=0}^{2n} \omega_i^c \left[\hat{\mathbf{z}}_{k|k-1} - \mathbf{z}_{k|k-1}^- \right] \left[\hat{\mathbf{z}}_{k|k-1} - \mathbf{z}_{k|k-1}^- \right]^T + \mathbf{R}_k \\ \mathbf{P}'_{xz,k} &= \sum_{i=0}^{2n} \omega_{(i)}^c \left[\hat{\mathbf{x}}_{k|k-1} - \mathbf{x}_{k|k-1}^- \right] \left[\hat{\mathbf{z}}_{k|k-1} - \mathbf{z}_{k|k-1}^- \right]^T\end{aligned}\quad (25)$$

where the measurement covariance matrix \mathbf{R}_k is determined based on sensor accuracy, and can be finally adjusted based on real-time estimation performance.

(5) Fading factor calculation

The unscented Kalman filtering (UKF) has the same weights for the system states at each instant k in the unscented transform. The system states at each instant k have the same effect on the predicted states, which leads to the prediction covariance matrix $\mathbf{P}_{k|k-1}$ gradually losing its corrective function on the system states. Once the system estimation error converges, the potential model uncertainty or external disturbances would result in the measurements failing to update the estimates and thus leading to UKF instability. To address this issue, the combination of the unscented Kalman filter and the strong tracking filter [36] forms a STUKF [37]. The STUKF redefines the prediction covariance matrix $\mathbf{P}_{k|k-1}$ by employing a suboptimal fading factor [38] $\Lambda = \text{diag}(\zeta_{1,k}, \zeta_{2,k}, \dots, \zeta_{n,k})$. The suboptimal fading factor in the time-varying filter gain matrix is deduced by

$$\begin{aligned}\mathbf{P}_{k|k-1} &= \Lambda_k \mathbf{P}'_{k|k-1} \\ \mathbf{P}_{zz,k} &= \Lambda_k \mathbf{P}'_{zz,k} \\ \mathbf{P}_{xz,k} &= \Lambda_k \mathbf{P}'_{xz,k}\end{aligned}\quad (26)$$

where the fading factor ζ_k can be calculated by

$$\begin{aligned}\zeta_{i,k} &= \frac{\text{tr}[\eta \mathbf{V}_{k-\varepsilon} \mathbf{R}_k]}{\text{tr}[\mathbf{P}'_{zz,k}]} \\ \zeta_{i,k} &= \begin{cases} 1 & \zeta_{i,k} \leq 1 \\ \zeta_{i,k} & \zeta_{i,k} > 1 \end{cases} \\ \mathbf{V}_k &= \begin{cases} \mathbf{v}_{k-1} \mathbf{v}_{k-1}^T & k = 0 \\ \frac{\rho_s \mathbf{V}_{k-1} + \mathbf{v}_{k-1} \mathbf{v}_{k-1}^T}{1 + \rho_s} & k \geq 1 \end{cases}\end{aligned}\quad (27)$$

where $0 < \rho_s < 0$ is the fading coefficient.

(6) Optimal estimation

$$\begin{aligned}\hat{\mathbf{x}}_k &= \hat{\mathbf{x}}_{k|k-1} + \mathbf{K}_k (\hat{\mathbf{z}}_k - \hat{\mathbf{z}}_{k|k-1}) \\ \mathbf{K}_k &= \mathbf{P}_{xz,k-1} \mathbf{P}'_{zz,k-1}^{-1} \\ \mathbf{P}_k &= \mathbf{P}_{k|k-1} - \mathbf{K}_k \mathbf{P}'_{zz,k-1} \mathbf{K}_k^T\end{aligned}\quad (28)$$

B. Tire Force Estimation

1) *Vertical Tire Force Estimation*: Suspension is a typical nonlinear system and here the STUKF is employed for vertical tire force estimation. A nonlinear discrete-time state representation of the suspension system is expressed as Equation (17). For a single suspension, it is assumed that the spring and damper have the same compression and compression rate, which can be directly measured by the suspension height sensor (see Fig. 1(a)). To reduce system dimensions and improve computing efficiency, the vertical tire force is estimated separately for each corner. The input vector \mathbf{u}_k is null. Take the compression, compression rate and tire vertical force as the system states, and the state vector at each time step k can be given by

$$\begin{aligned}\mathbf{x}_k^z &= [\Delta z, \Delta \dot{z}, F_z^i]^T \\ &= [x_{1,k}^z, x_{2,k}^z, x_{3,k}^z]^T\end{aligned}\quad (29)$$

Considering that the inertia force of the unsprung mass is much smaller than that of the vertical tire force, its influence on vertical tire force estimation can be ignored here. According to Equation (3), the nonlinear function $f^z(\cdot)$ for vertical tire force estimation can be deduced by

$$f^z = \begin{cases} f_1^z = x_{1,k-1}^z \\ f_2^z = x_{2,k-1}^z + x_{1,k-1}^z \cdot \Delta T \\ f_3^z = k_s^i \cdot x_{2,k-1}^z + c_s^i(z_{1,k-1}^z) \cdot x_{1,k-1}^z \\ + F_{cam}^i(x_{1,k-1}^z, x_{2,k-1}^z) + m_u^i g \end{cases}\quad (30)$$

The measurements $\mathbf{z}_k \in \mathbb{R}^2$ at time step k can be given by

$$\mathbf{z}_k^z = [\Delta z, \Delta \dot{z}]^T \quad (31)$$

The observation functions $h^z(\cdot)$ is linear and can be given by

$$h^z = \begin{cases} h_1^z = x_{1,k-1}^z \\ h_2^z = x_{2,k-1}^z \end{cases}\quad (32)$$

2) *Lateral Tire Force Estimation*: Accurate lateral tire force estimation is important for vehicle lateral stability assessment. According to Equations (8), (9) and (17), a nonlinear discrete state-space equation for lateral tire force estimation can be established. Take the lateral acceleration and yaw acceleration of the vehicle and the four lateral tire forces as the system states, which can be given by

$$\begin{aligned}\mathbf{x}_k^y &= [a_y, \dot{\omega}_z, F_y^{L1}, F_y^{R1}, F_y^{L2}, F_y^{R2}] \\ &= [x_{1,k}^y, x_{2,k}^y, x_{3,k}^y, x_{4,k}^y, x_{5,k}^y, x_{6,k}^y]\end{aligned}\quad (33)$$

The input vector \mathbf{u}_k consists of the front-wheel steering angle, the longitudinal tire forces of the front wheels and the vertical tire forces of the four wheels, which can be given

by

$$\begin{aligned} \mathbf{u}_k^y &= [\delta_k, F_{x,k}^{L1}, F_{x,k}^{R1}, F_{z,k}^{L1}, F_{z,k}^{R1}, F_{z,k}^{L2}, F_{z,k}^{R2}] \\ &= [u_{1,k}^y, u_{2,k}^y, u_{3,k}^y, u_{4,k}^y, u_{5,k}^y, u_{6,k}^y, u_{7,k}^y] \end{aligned} \quad (34)$$

The front-wheel steering angle is measured by the steering angle encoder while the vertical tire forces are estimated as presented in Section III B 1). The derivation of the longitudinal tire forces are presented in Section III B 3).

The system measurements include the lateral and yaw accelerations, which are given by

$$\mathbf{z}_k^y = [z_{1,k}^y, z_{2,k}^y]^T = [a_y, \dot{\omega}_z]^T \quad (35)$$

The nonlinear function based on the random-walk model for lateral tire force estimation can be given by

$$f^y = \begin{cases} f_1^y = \frac{1}{m} \left((x_{3,k-1}^y + x_{4,k-1}^y) \cos(u_{1,k}^y) + x_{5,k-1}^y \right) \\ f_2^y = x_{2,k-1}^y \\ f_3^y = \frac{(x_{1,k-1}^y + x_{2,k-1}^y L_a) u_{4,k}^y}{g} \\ f_4^y = \frac{(x_{1,k-1}^y + x_{2,k-1}^y L_a) u_{3,k}^y}{g} \\ f_5^y = \frac{(x_{1,k-1}^y - x_{2,k-1}^y L_b) u_{6,k}^y}{g} \\ f_6^y = \frac{(x_{1,k-1}^y - x_{2,k-1}^y L_b) u_{7,k}^y}{g} \end{cases} \quad (36)$$

According to Equation (35), the observation function $h^y(\cdot)$ can be given by

$$h^y = \begin{cases} h_1^y = x_{1,k-1}^y \\ h_2^y = x_{2,k-1}^y \end{cases} \quad (37)$$

3) *Longitudinal Tire Force Estimation*: Considering that the output torque and rotational speed of each wheel can be obtained from the motor control unit, a widely used classic Kalman filter is employed for linear longitudinal tire force estimation based on the random-walk model (Equation (13)). Consider a discrete time-varying linear control system as

$$\begin{cases} \mathbf{x}_k^x = \mathbf{A}\mathbf{x}_{k-1}^x + \mathbf{B}\mathbf{u}_k^x + \mathbf{w}_k^x \\ \mathbf{z}_k^x = \mathbf{H}\mathbf{x}_k^x + \mathbf{v}_k^x \end{cases} \quad (38)$$

where $\mathbf{x}_k^x \in \mathbb{R}^n$ is the state vector; $\mathbf{u}_k^x \in \mathbb{R}^p$ is the control input; $\mathbf{z}_k^x \in \mathbb{R}^m$ is the measurement; $\mathbf{w}_k^x \in \mathbb{R}^r$ and $\mathbf{v}_k^x \in \mathbb{R}^m$ are the white noises; \mathbf{A} and \mathbf{B} are the state transition and input matrices, respectively.

For a single wheel, taking the wheel torque as the input and the wheel angular speed, angular acceleration and longitudinal force as the states, the state vector can be given by

$$\begin{aligned} \mathbf{x}_k^x &= [F_x^i, \omega^i, \dot{\omega}^i]^T \\ &= [x_{1,k}^x, x_{2,k}^x, x_{3,k}^x]^T \end{aligned} \quad (39)$$

\mathbf{A} and \mathbf{B} can be expressed by

$$\mathbf{A} = \begin{bmatrix} 0 & 0 & -\frac{R_e}{J_\omega} \\ 0 & 1 & \Delta T \\ 0 & 0 & 1 \end{bmatrix}, \quad \mathbf{B} = \begin{bmatrix} -\frac{1}{R_e} \\ 0 \\ 0 \end{bmatrix} \quad (40)$$

where ΔT is the sampling time.

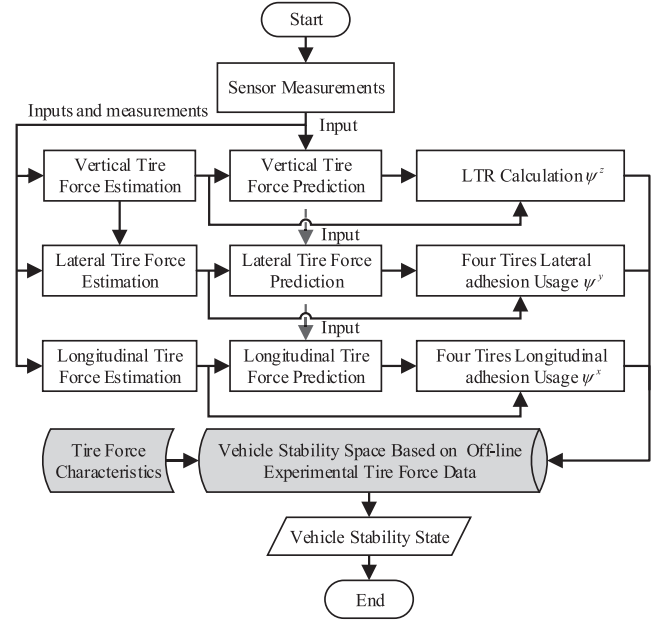


Fig. 4. The schematic diagram of the proposed vehicle stability assessment and prediction system.

The measurement z_k^x is the wheel rotational speed, which is equal to the rotational speed of in-wheel motor as

$$z_k^x = \omega^i = z_{2,k}^x \quad (41)$$

and $\mathbf{H}=[0, 1, 0]$ is the observation matrix.

C. Vehicle Stability Assessment and Prediction System

1) *Vehicle Stability Assessment System*: Vehicle stability assessment is essential for active safety control and is used to trigger safety control actions and to synthesize specific control targets for chassis coordinated control. Vehicle stability is essentially a comprehensive indication of four tires' force states. The full X-by-wire chassis coordinated control for enhancing vehicle safety and stability needs to be achieved through tire forces. Therefore, it is necessary to establish a tire force based comprehensive vehicle stability assessment system to evaluate the vehicle longitudinal, yaw and roll stability for triggering specific safety control actions. According to the effective working areas of different X-by-wire actuators, the vehicle stability can be divided into five states. The schematic diagram of the proposed vehicle stability assessment and prediction system is shown in Fig. 4. The presented vehicle stability assessment system first estimates the vertical and longitudinal tire forces, which are further used for lateral tire force estimation. Based on the driver's inputs and sensor measurements, the tire force states can be predicted for a short period. For vehicle roll stability, four wheels' vertical forces are used for LTR calculation, and the reading of the LTR larger than a pre-set value is defined as rollover instability. The estimated four wheels' longitudinal and lateral tire forces are normalized to form four tire friction ellipses, each of which can be divided into four stability regions according to the relationship between vehicle planar motion state

and tire dynamic characteristics. Based on the four tire friction ellipses and the LTR value, a comprehensive vehicle stability assessment and prediction system is established based on tire force testing data.

The LTR index utilizes the ratio of the difference of the left and right tire vertical loads over the overall vertical load to quantitatively evaluate vehicle rollover propensity, which can be given by

$$\Psi^z = \frac{F_z^{R1} + F_z^{R2} - F_z^{L1} - F_z^{L2}}{F_z^{L1} + F_z^{L2} + F_z^{R1} + F_z^{R2}} \quad (42)$$

The LTR index ranges from -1 to 1, and -1 means the right tires are lifted off the ground while 1 indicates the lift-off of the left tires. An LTR value of 0 means both sides have the same vertical load with no rollover tendency.

To evaluate vehicle longitudinal and yaw stability, the longitudinal and lateral tire adhesion usage indexes are respectively established, which are given by

$$\Psi^x = \frac{F_x^i}{\mu F_z^i}, \quad \Psi^y = \frac{F_y^i}{\mu F_z^i} \quad (43)$$

where μ is the tire-road friction coefficient. Readers can refer to Ref. [28] for more details on tire-road friction estimation.

According to Equations (42) and (43), the vehicle longitudinal, yaw and roll stability space can be defined as

$$\Omega = \Upsilon(\Psi^x, \Psi^y, \Psi^z) \quad (44)$$

a) Longitudinal and yaw stability analysis: The tire's longitudinal and lateral combined slip characteristics can be obtained as shown in Fig. 5(a) and (b). Fig. 5(a) shows the relationship between longitudinal tire force and tire slip ratio under different tire sideslip angles. The evolution of the longitudinal tire force can be divided into two zones, i.e., the stable and saturation zones. The stable zone is defined as the area from the zero to the peak point of the longitudinal tire force. It is worth noted that the nonlinear characteristic has no effect on vehicle ride comfort and handling performance despite that the longitudinal tire force in the stable zone exhibits initially linear and later nonlinear characteristics. Thus, the linear and nonlinear regions are defined as the stable zone. After the peak point, the longitudinal tire force reaches saturation, and exhibits a decline trend with the increasing tire slip ratio. In the saturation zone, the lateral tire force is also reduced to a minimum within the tire-road friction constraint. Even there is a slight steering, the vehicle may endure severe side slip or spin. Under such circumstance, the vehicle longitudinal active control systems such as ASR or ABS need to be triggered.

Fig. 5(b) depicts the evolutions of the lateral tire force and of the tire sideslip angle under different slip ratios. Considering the effect of lateral tire force on the steering characteristics, the lateral tire force can be separated into three zones, i.e., the linear, the transition and the saturation zone. In the linear zone, the lateral tire force presents a linear relationship with the tire sideslip angle (see Fig. 5(b)), and the steering system also presents a linear response to the wheel steer angle input. The AFS system can enhance the handling performance by applying an extra front-wheel steer angle in the linear zone. In the transition zone, the lateral tire force exhibits strong nonlinearity, and the vehicle steering response gradually exhibits a nonlinear

relationship. In the zone, the AFS and the DYC system can work cooperatively with their respective advantages for better control effect. In the saturation zone, the lateral tire force reaches the peak, and the vehicle steering response is insensitive to the steering angle so that the DYC system works solely in this zone.

According to Equation (43), the longitudinal and lateral tire forces can be normalized and form the friction ellipse as shown in Fig. 5(c), and the five zones in Fig. 5(a) and Fig. 5(b) can also be mapped into four stability states (Zone I - Zone IV).

Zone I represents the stable region, where the longitudinal and lateral tire forces are small and the vehicle has a large stability margin. Zone II is the transition zone, where the lateral tire force is larger than that in Zone I and exhibits certain nonlinear characteristics. Zone III is the yaw instability zone, where the tire force exhibits strong nonlinearity and is prone to saturation. Zone IV is the longitudinal instability zone, where the longitudinal tire force reaches its limits.

Upon a close observation on Fig. 5(c), the stability state can be divided by the elliptic and hyperbolic equations, which are given by

$$\begin{aligned} \left(\frac{\Psi^x}{\Psi_n^x}\right)^2 + \left(\frac{\Psi^y - \Delta\Psi_n^y}{\Psi_n^y}\right)^2 &= \Psi_n^c \\ \left(\frac{\Psi^x}{\Psi_4^x}\right)^2 - \left(\frac{\Psi^y}{\Psi_4^y}\right)^2 &= \Psi_4^c \end{aligned} \quad (45)$$

where Ψ_n^x , Ψ_n^y and Ψ_n^c denote the parameters of the corresponding elliptic equation; $\Delta\Psi_n^y$ is the offset of the ellipse on the Ψ^y axis; the subscript $n \in \{1, 2, 3\}$ represent the stable, transition and saturation elliptic equations; Ψ_4^x , Ψ_4^y and Ψ_4^c are the parameters of the hyperbolic equation. Thus, the vehicle stability Zone I to IV can be expressed by Equations (46)-(49).

For Zone I, the numerical expression can be given by

$$\begin{aligned} -\Psi_4^x \cdot \sqrt{\Psi_4^c + \left(\frac{\Psi^y}{\Psi_4^y}\right)^2} &\leq \Psi^x \leq \Psi_4^x \cdot \sqrt{\Psi_4^c + \left(\frac{\Psi^y}{\Psi_4^y}\right)^2} \\ -\Psi_1^y \cdot \sqrt{\Psi_1^c - \left(\frac{\Psi^x}{\Psi_1^x}\right)^2} - \Delta\Psi_1^y &\leq \Psi^y \leq \Psi_1^y \cdot \sqrt{\Psi_1^c - \left(\frac{\Psi^x}{\Psi_1^x}\right)^2} + \Delta\Psi_1^y \end{aligned} \quad (46)$$

Zone II can be expressed by

$$\begin{aligned} -\Psi_4^x \cdot \sqrt{\Psi_4^c + \left(\frac{\Psi^y}{\Psi_4^y}\right)^2} &\leq \Psi^x \leq \Psi_4^x \cdot \sqrt{\Psi_4^c + \left(\frac{\Psi^y}{\Psi_4^y}\right)^2} \\ \Psi_1^y \cdot \sqrt{\Psi_1^c - \left(\frac{\Psi^x}{\Psi_1^x}\right)^2} + \Delta\Psi_1^y &\leq \Psi^y \leq \Psi_2^y \cdot \sqrt{\Psi_2^c - \left(\frac{\Psi^x}{\Psi_2^x}\right)^2} + \Delta\Psi_2^y \\ -\Psi_2^y \cdot \sqrt{\Psi_2^c - \left(\frac{\Psi^x}{\Psi_2^x}\right)^2} - \Delta\Psi_2^y &\leq \Psi^y \leq -\Psi_1^y \cdot \sqrt{\Psi_1^c - \left(\frac{\Psi^x}{\Psi_1^x}\right)^2} - \Delta\Psi_1^y \end{aligned} \quad (47)$$

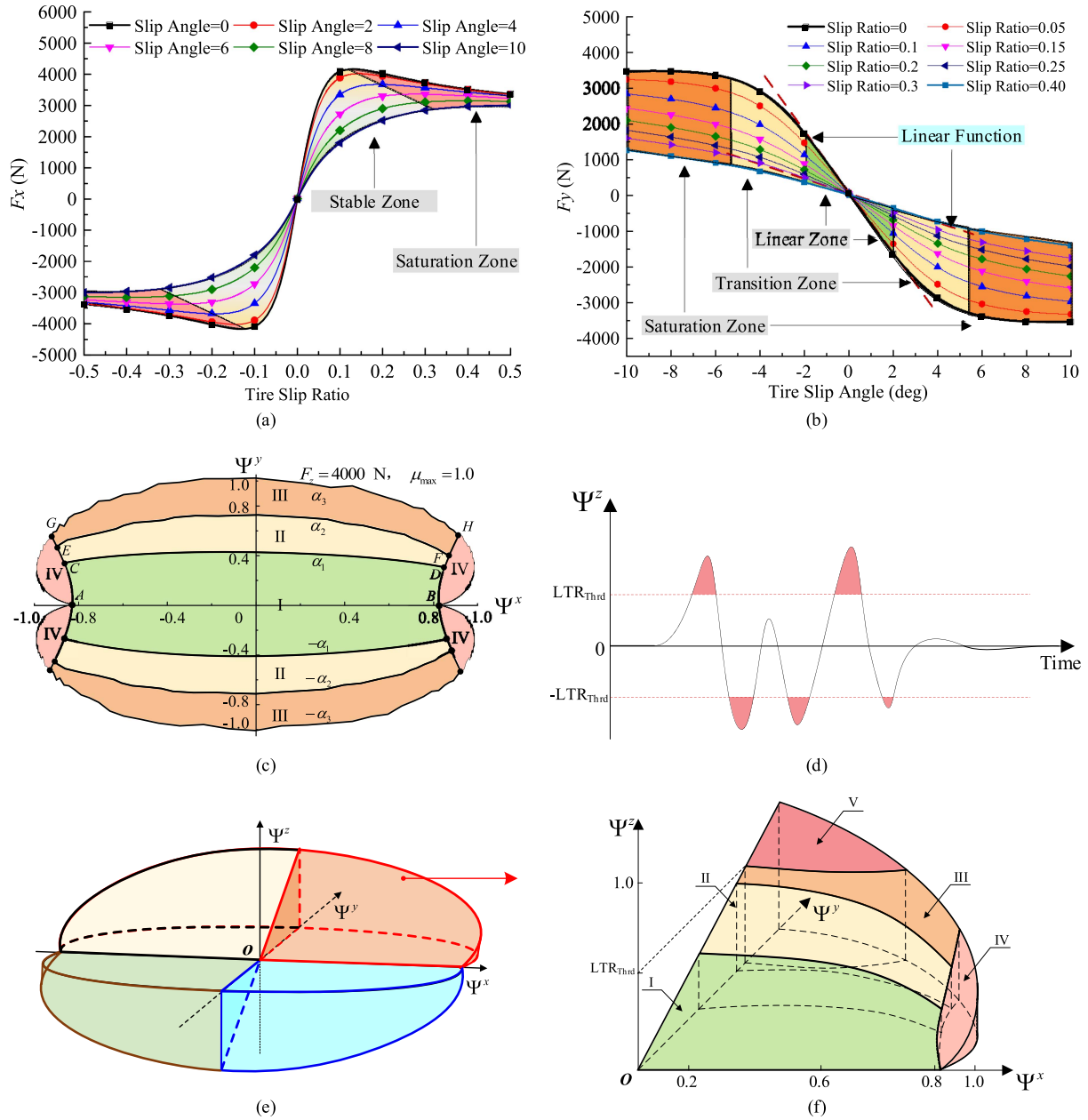


Fig. 5. The development of the proposed vehicle stability space: (a) and (b) the tire longitudinal and lateral combined slip characteristics; (c) the adhesion ellipse; (d) the LTR value during specific maneuvers; (e) the vehicle stability space; (f) a quarter of the vehicle stability space.

The numerical expression of Zone III can be given by

$$-\Psi_4^x \cdot \sqrt{\Psi_4^c + \left(\frac{\Psi^y}{\Psi_4^y}\right)^2} \leq \Psi^x \leq \Psi_4^x \cdot \sqrt{\Psi_4^c + \left(\frac{\Psi^y}{\Psi_4^y}\right)^2}$$

$$\Psi_2^y \cdot \sqrt{\Psi_2^c - \left(\frac{\Psi^x}{\Psi_2^x}\right)^2} + \Delta\Psi_2^y \leq \Psi^y \leq \Psi_3^y.$$

$$\sqrt{\Psi_3^c - \left(\frac{\Psi^x}{\Psi_3^x}\right)^2} + \Delta\Psi_3^y$$

$$-\Psi_3^y \cdot \sqrt{\Psi_3^c - \left(\frac{\Psi^x}{\Psi_3^x}\right)^2} - \Delta\Psi_3^y \leq \Psi^y \leq -\Psi_2^y.$$

$$\sqrt{\Psi_2^c - \left(\frac{\Psi^x}{\Psi_2^x}\right)^2} - \Delta\Psi_2^y \quad (48)$$

Zone IV can be expressed by

$$\Psi^x \leq -\Psi_4^x \cdot \sqrt{\Psi_4^c + \left(\frac{\Psi^y}{\Psi_4^y}\right)^2}$$

$$\Psi^x \geq \Psi_4^x \cdot \sqrt{\Psi_4^c + \left(\frac{\Psi^y}{\Psi_4^y}\right)^2} \quad (49)$$

b) Roll stability analysis: Vehicle yaw and roll stabilities are coupled with each other. There are two premises for vehicle rollover occurrence. Ignoring the effect of the CG lateral offset,

a static vehicle rollover stability index can be defined as

$$a_y^{Thd} = \frac{Bg}{2h_g} \quad (50)$$

where a_y^{Thd} is the static vehicle rollover index. It ignores the elastic effect of the suspension and represents the maximum lateral acceleration before rollover occurrence under steady state conditions; h_g is the vertical distance from the CG to the ground; B denotes the track width. In normal driving conditions, the maximum vehicle lateral acceleration is determined by the peak road adhesion coefficient μ_{\max} . When $a_y^{Thd} > \mu_{\max}g$, the vehicle wouldn't roll over in any case under non-tripping conditions. Thus, the lateral acceleration threshold index can be employed to determine the vehicle rollover potential. Only when $a_y^{Thd} < \mu_{\max}g$ will the LTR value be used to evaluate the rollover stability.

As shown in Fig. 5(d), the LTR index is utilized to evaluate vehicle dynamic rollover stability with an LTR value greater than the preset value meaning an imminent rollover. This preset value can be obtained through tests for a specific vehicle model. In fact, one wheel may lift off the road when the absolute value of LTR is larger than 0.9 despite that the vehicle doesn't completely roll over. Thus, a lower value such as LTR=0.7 should be set as the threshold to activate the rollover stability system [17]. So, the vehicle stability zone can be extended from the 2-D plane to a 3-D space as shown in Fig. 5(e). Considering the first quadrant of the 3-D stability space as shown in Fig. 5(f), Zone V can be deduced as follows.

According to Equation (4), the LTR can be deduced by

$$\Psi^z = \frac{2}{mgB} (k_\varphi \varphi + c_\varphi \dot{\varphi}) = \frac{2m_s h_{rc}}{mgB} (g\varphi + a_y) - \frac{2I_x \ddot{\varphi}}{mgB} \quad (51)$$

Considering $\frac{2I_x \ddot{\varphi}}{mgB} \approx 0$ during daily driving conditions [17] and $\varphi = \rho_\varphi \cdot a_y \cdot \tau(s)$ [39], ρ_φ denotes the proportionality coefficient, and $\tau(s)$ is the transfer function. Thus, the LTR can be approximated as

$$\Psi^z = \frac{2m_s h_{rc}}{mgB} (g \cdot \rho_\varphi \cdot \tau(s) + 1) a_y \quad (52)$$

Based on Equations (9) and (43), the lateral acceleration can be expressed by

$$a_y = \mu_{\max} \cdot g \cdot \Psi^y \quad (53)$$

The relationship between Ψ^z and Ψ^y can be given by

$$\Psi^z = \frac{2m_s h_{rc} \mu_{\max}}{mB} (g \cdot \rho_\varphi \cdot \tau(s) + 1) \cdot \Psi^y \quad (54)$$

The stability Zone V can be expressed by Equation (55).

The stability Zone V can be expressed by

$$\begin{aligned} \Psi_0^y \leq \Psi^y \leq \Psi_3^y \cdot \sqrt{\Psi_3^c - \left(\frac{\Psi^x}{\Psi_3^x}\right)^2} + \Delta\Psi_3^y \\ - \Psi_3^y \cdot \sqrt{\Psi_3^c - \left(\frac{\Psi^x}{\Psi_3^x}\right)^2} - \Delta\Psi_3^y \leq \Psi^y \leq \Psi_0^y \end{aligned}$$

$$\begin{aligned} \Psi^z \geq \frac{2m_s h_{rc} \mu_{\max}}{mL} (g \cdot \rho_\varphi \cdot \tau(s) + 1) \cdot \Psi_0^y, \quad \Psi^z \\ \leq -\frac{2m_s h_{rc} \mu_{\max}}{mL} (g \cdot \rho_\varphi \cdot \tau(s) + 1) \cdot \Psi_0^y \end{aligned} \quad (55)$$

where Ψ_0^y is the lateral tire adhesion usage index corresponding to the preset LTR value.

2) *Vehicle Stability Prediction System*: Vehicle stability prediction system aims to evaluate vehicle stability in a certain timeline and to enable VSCs in time. The tire force estimation and prediction employ the same dynamics model. The difference in between lies in that the tire force estimator achieves state estimation via measurement updates at each time step while the tire force predictor utilizes current driver's inputs including acceleration/braking acceleration and steering angle rate and vehicle roll state as the inputs to predict the tire force states in a short period. Herein, the driver's reaction time is selected as the prediction horizon. For ordinary drivers, their action time is usually less than 0.5 s so that this study set 0.5 s as the prediction time.

Consider the discrete equation of the control system as

$$\begin{cases} \mathbf{x}_k = \bar{\mathbf{A}}\mathbf{x}_{k-1} + \bar{\mathbf{B}}\mathbf{u}_{k-1} \\ \mathbf{y}_k = \bar{\mathbf{C}}\mathbf{x}_k \end{cases} \quad (56)$$

where $\bar{\mathbf{A}}$ and $\bar{\mathbf{B}}$ are the system transition and input matrices; \mathbf{u}_{k-1} is the system input.

Define $N_p \geq 1$ as the predictive horizon at time step k , the system state \mathbf{X}_k and the control input \mathbf{U}_k are given by

$$\mathbf{X}_k = \begin{bmatrix} \mathbf{x}_{k+1|k} \\ \mathbf{x}_{k+2|k} \\ \vdots \\ \mathbf{x}_{k+N_p|k} \end{bmatrix}, \mathbf{U}_k = \begin{bmatrix} \mathbf{u}_{k|k} \\ \mathbf{u}_{k+1|k} \\ \vdots \\ \mathbf{u}_{k+N_p-1|k} \end{bmatrix} \quad (57)$$

where $k + N_p|k$ represents the prediction at time step $k + N_p$ based on the information available at time step k .

At time step k , the system state \mathbf{x}_k can be updated using

$$\mathbf{X}_k = \Phi \mathbf{x}_k + \Theta \mathbf{U}_k \quad (58)$$

where Φ and Θ can be calculated by

$$\Phi = \begin{bmatrix} \bar{\mathbf{A}}^1 \\ \bar{\mathbf{A}}^2 \\ \vdots \\ \bar{\mathbf{A}}^{N_p} \end{bmatrix}, \Theta = \begin{bmatrix} \bar{\mathbf{A}}^{1-1} \bar{\mathbf{B}} & \dots & 0 & 0 \\ \bar{\mathbf{A}}^{2-1} \bar{\mathbf{B}} & \bar{\mathbf{A}}^{2-2} \bar{\mathbf{B}} & \dots & 0 \\ \vdots & \vdots & \ddots & \vdots \\ \bar{\mathbf{A}}^{N_p-1} \bar{\mathbf{B}} & \bar{\mathbf{A}}^{N_p-2} \bar{\mathbf{B}} & \dots & \bar{\mathbf{A}}^{N_p-N_p} \bar{\mathbf{B}} \end{bmatrix} \quad (59)$$

a) Longitudinal Tire Force Prediction

For longitudinal tire force prediction, it is necessary to introduce the driver's intention recognition model. This model maps the relationship between accelerator/brake pedal position and vehicle longitudinal acceleration. According to vehicle longitudinal dynamics model, the relationship between the accelerator/brake pedal and the total output torque can be obtained.

Considering the ride comfort and braking torque response characteristics, a torque ramp is given by

$$T_{d,k}^i = \begin{cases} T_{d,k-1}^i + \Delta & \text{if } T_{d,k,\text{demd}}^i - T_{d,k-1}^i > \Delta \\ T_{d,k,\text{demd}}^i & \text{else} \end{cases} \quad (60)$$

where $T_{d,k,\text{demd}}^i$ denotes the driver's torque demand (driver's intention) at time step k ; Δ is the predefined torque ramp. During hard accelerations, the input within a predictive horizon of N_p can be derived as

$$\mathbf{U}_k^x = \begin{bmatrix} u_{k|k}^x \\ u_{k+1|k}^x \\ \vdots \\ u_{k+N_p-1|k}^x \end{bmatrix} = \begin{bmatrix} T_{d,k}^i \\ T_{d,k}^i + \Delta \\ \vdots \\ T_{d,k}^i + (N_p - 1)\Delta \end{bmatrix} \quad (61)$$

The longitudinal tire force can be predicted based on Equation (40). It should be noted that the input is $u_1 = u_2 = \dots = u_{N_p}$ for a uniform motion.

b) *Lateral Tire Force Prediction* According to Equations (8) and (10), the lateral tire force predictor is given by

$$a_y = \frac{C_\alpha^f}{m} \left(\beta + \frac{L_a \omega_z}{v_x} \right) + \frac{C_\alpha^r}{m} \left(\beta - \frac{L_b \omega_z}{v_x} \right) - \frac{C_\alpha^f}{m} \delta$$

$$\dot{\omega}_z = \frac{L_a C_\alpha^f}{I_z} \left(\beta + \frac{L_a \omega_z}{v_x} \right) - \frac{L_b C_\alpha^r}{I_z} \left(\beta - \frac{L_b \omega_z}{v_x} \right) - \frac{L_a C_\alpha^f}{I_z} \delta \quad (62)$$

where the system input is the front-wheel steering angle. The rotational angle of the steering wheel needs to be predicted based on the lateral tire force estimator. The steering angle encoder can measure the steering angle and the steering rate $\dot{\delta}_k$ at the same time. The vehicle sideslip angle can be estimated based on our previous work, and readers can refer to Ref. [40] for more technical details. The input of the predictor can be expressed as

$$\mathbf{U}_k^y = \begin{bmatrix} u_{k|k}^y \\ u_{k+1|k}^y \\ \vdots \\ u_{k+N_p-1|k}^y \end{bmatrix} = \begin{bmatrix} \delta_k \\ \delta_k + \Delta T \dot{\delta}_k \\ \vdots \\ \delta_k + (N_p - 1)\Delta T \dot{\delta}_k \end{bmatrix} \quad (63)$$

$$\mathbf{X}_k^y = \begin{bmatrix} x_{k+1|k}^y \\ x_{k+2|k}^y \\ \vdots \\ x_{k+N_p|k}^y \end{bmatrix} = \begin{bmatrix} a_{y,k+1|k} \\ a_{y,k+2|k} \\ \vdots \\ a_{y,k+N_p|k} \end{bmatrix} \quad (64)$$

The prediction of the lateral tire forces can be achieved using the lateral tire force estimator.

c) *Vertical Tire Force Prediction*: Vehicle roll state prediction is key to vertical tire force estimation. The IMU can measure the vehicle roll rate and roll acceleration, and the relationship between vertical suspension displacement and vehicle roll angle can be obtained based on Equation (7). The vehicle roll angle

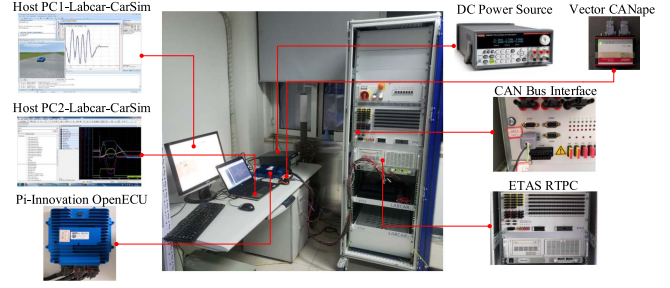


Fig. 6. The Hardware-in-the-Loop platform.

and roll rate in a short period can be predicted by

$$\mathbf{y}_k^\varphi = \begin{bmatrix} y_{k|k}^\varphi \\ y_{k+1|k}^\varphi \\ \vdots \\ y_{k+N_p-1|k}^\varphi \end{bmatrix} = \begin{bmatrix} \begin{bmatrix} \varphi_k \\ \dot{\varphi}_k \end{bmatrix} \\ \begin{bmatrix} \varphi_k + \dot{\varphi}_k \Delta T \\ \dot{\varphi}_k + \ddot{\varphi}_k \Delta T \end{bmatrix} \\ \vdots \\ \begin{bmatrix} \varphi_k + (N_p - 1)\Delta T \dot{\varphi}_k \\ \dot{\varphi}_k + (N_p - 1)\Delta T \ddot{\varphi}_k \end{bmatrix} \end{bmatrix} \quad (65)$$

$$\mathbf{y}_k^z = \Upsilon^i (\mathbf{y}_k^\varphi) \quad (66)$$

The vertical tire force prediction can be realized combining Equation (57) with the vertical tire force estimator.

IV. EXPERIMENTS AND DISCUSSIONS

The performance of the proposed vehicle stability assessment and prediction system is examined based on a Hardware-in-the-Loop (HIL) platform as shown in Fig. 6. This platform consists of two host computers, a real-time personal computer (RTPC), a CANape, an Open ECU and a DC power source. The host computer PC-1 is used to configure the vehicle dynamics model and sensors and to generate the executable file by integrating the vehicle dynamics model in Carsim with the LabCar project. The host PC-2 is used to compile the proposed vehicle stability assessment system in the Matlab/Simulink into the executable code in the Open ECU. The RTPC runs the executable file obtained from PC-1 and also serves as a high-fidelity vehicle to provide vehicle dynamics response signals and sensor measurements. The measurement accuracy, mounting error and dynamic characteristics of the used sensors are set as shown in Table II. The front/rear suspension damping coefficient is shown in Fig. 7. The communication between the RTPC and the OPEN ECU is realized through the CAN, and the CANape is employed for application download, CAN bus data logging and parameters calibration. The computational frequency of the proposed system in the Open ECU is set as 100 Hz while the sampling frequency of the vehicle sensors in the Carsim run in the RTPC is set as 1000 Hz. The specifications of the Open ECU are shown in Table III. The hybrid maneuver combining the slalom and hard acceleration on low adhesion road with the double lane change (DLC) maneuver and a fish hook procedure are used to simulate critical driving conditions. Detailed specifications of the test vehicle are listed in Table II.

TABLE II
PARAMETERS OF THE VEHICLE MODEL

Name	Value (Unit)
Vehicle sprung mass (with two passengers) m_s	1617 kg
Vehicle unsprung mass (each corner) m_u	80 kg
Moment of inertia about the roll axis I_x	700.7 kg · m ²
Displacement between left and right suspension mounting positions l	1.170 m
Height of the center of mass h	0.650 m
Displacement from sprung mass CG to roll center h_{rc}	0.330 m
Tread width B_f, B_r	1.565 m, 1.550 m
Front/Rear suspension damping coefficient c_s^f, c_s^r	see Fig. 7
Front/Rear suspension spring stiffness k_s^f, k_s^r	-60000 N/rad
Moment of inertia about the yaw axis I_z	2 592.2 kg · m ²
Length from the CG to the front/rear axis L_a, L_b	1.35 m, 1.31 m
Tire cornering stiffness C_α^j	-60000 N/rad
Tire effective radius R_e	0.321 m
Moment of inertia of the wheel J_ω	0.84 kg · m ²

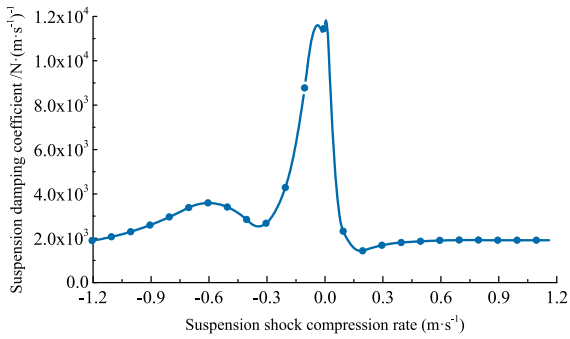


Fig. 7. The suspension damping coefficient.

TABLE III
SPECIFICATIONS OF THE OPEN ECU

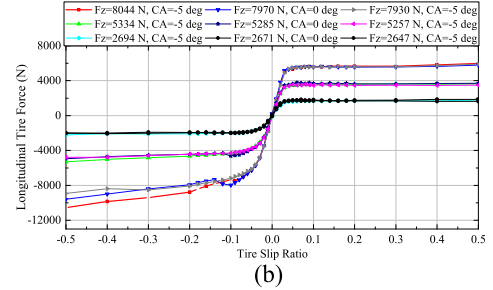
Name	Value (Unit)
Processor	NXP MPC5674F
Rate	264 MHz
Code space	3 MB
RAM space	256 KB
Calibration space	512 KB
Can channels	4

A. Vehicle Stability Space

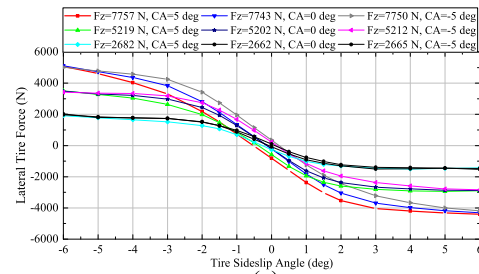
In order to establish an offline vehicle stability space, a tire testing experiment was conducted to investigate the dynamic characteristics of tire. As shown in Fig. 8(a), the used tire is 215/45ZR18 93 W with a tire pressure of 220 kpa. Three typical test conditions, i.e., pure longitudinal slip, pure side slip and combined slip, were considered with three different loads and tire camber angle settings. The test results under the pure longitudinal slip condition is shown in Fig. 8(b). The relationship between the longitudinal tire force and the tire slip ratio was obtained by changing the tire camber angle (CA) and vertical load (F_z). Fig. 8(c) shows the relationship between the lateral tire force and the tire slideslip angle under the pure side slip condition. In real driving conditions, the tire would endure



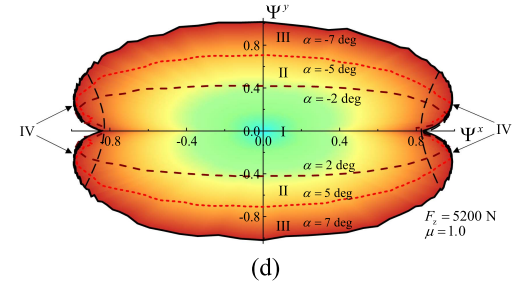
(a)



(b)



(c)



(d)

Fig. 8. The tire test results: (a) the tire test bench; (b) the tire test result under the pure longitudinal slip; (c) the tire test result under the pure side slip and (d) the tire adhesion ellipse under the combined slip.

combined slip conditions such as vehicle cornering together with hard accelerating or decelerating. The combined slip test result is shown in Fig. 8(d). It was developed by obtaining the longitudinal and lateral tire forces under combined slip conditions and by normalizing the tire forces based on Equation (45). Taking vehicle roll motion into consideration, the LTR threshold is set as ± 0.7 [17], and the vehicle stability space can be developed based on Fig. 8(d) and the set LTR thresholds.

B. The Hybrid Maneuver

The combined slalom and hard acceleration on low adhesion road and DLC maneuver is used to examine the performance of the presented scheme on vehicle longitudinal and yaw stability evaluation. In the scenario, the test vehicle travels from a slalom road onto a low adhesion road and then back to a DLC road. As shown in Fig. 9(a)-(c), different background colors represent different test scenarios. For brevity, only the left wheel of the front axle (L1) is selected to show the tire force estimation

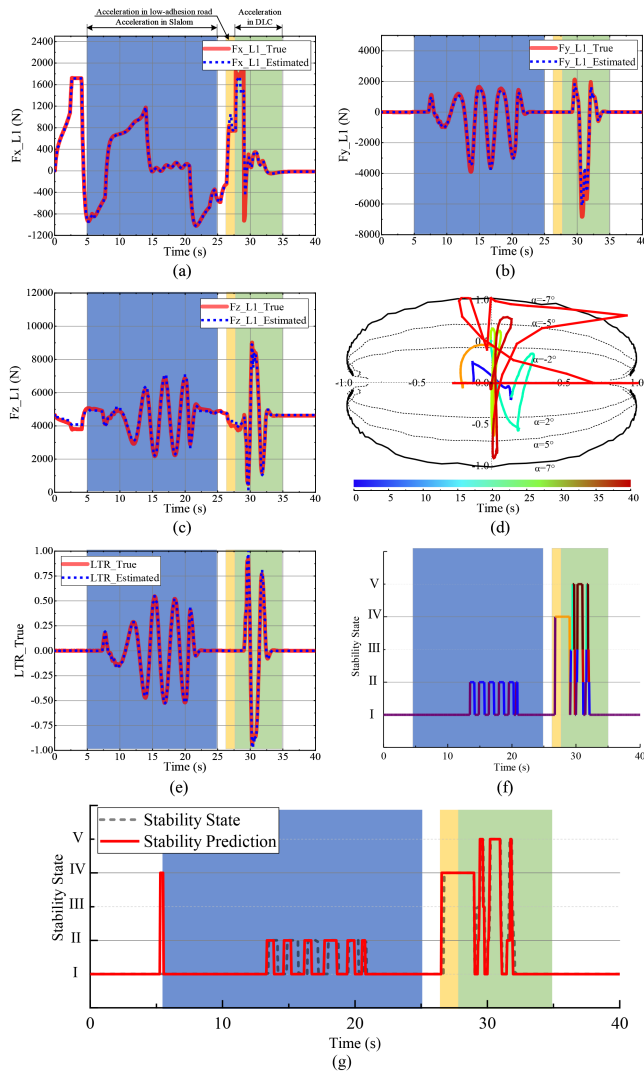


Fig. 9. The experimental results of the proposed comprehensive vehicle stability assessment system under hybrid maneuver: (a) the estimated longitudinal tire force; (b) the estimated lateral tire force; (c) the estimated vertical tire force; (d) the longitudinal and lateral adhesion usage; (e) the estimated LTR value; (f) the comprehensive vehicle stability state; (g) the predicted vehicle stability state.

performance. The proposed longitudinal, lateral and vertical tire force estimators can accurately track their respective true values throughout the test with the normalized root mean square errors of 1.62%, 1.04% and 1.43%. The distribution of the longitudinal and lateral tire adhesion usage in the friction ellipse is illustrated in Fig. 9(d). It can be seen that the vehicle motion covers all four stability regions during the entire test. The LTR evolution is depicted in Fig. 9(e), where the LTR exceeds the pre-set value of 0.7 only during the DLC stage. The vehicle stability can be evaluated in real-time with the comprehensive vehicle stability state delineated in Fig. 9(f). Seen from Fig. 9(f), when operating on the Slalom road, the test vehicle's stability jumps back and forth between State I and II. This means the AFS and the DYC system can work together to improve yaw stability and handling performance. Then, the test vehicle drives onto the low adhesion road, resulting in obvious wheel slip and thus the stability switching to State IV. In this state, the

vehicle longitudinal active control such as ASR needs to be triggered. Finally, the vehicle runs back onto the DLC road, and experiences rollover and yaw instability with the vehicle stability state entering State V due to the high vehicle velocity and sharp steering maneuver. Anti-rollover control action is required to prevent potential vehicle rollover. The vehicle stability prediction with a prediction horizon of 50 time steps is shown in Fig. 9(g), which represents a prediction time of 0.5 s. It is worth noted that this prediction is based on the current driver's inputs. Under extreme driving conditions, it bears enormous significance for improving vehicle safety if the vehicle stability assessment system can predict vehicle stability states in 0.2-0.5 s in advance.

C. The Fish Hook Procedure

The fish hook procedure is used to simulate the driver's response under the panic state to further examine the effectiveness of the proposed vehicle stability assessment system under extreme conditions. The whole test procedure can be divided into three stages. First, the test vehicle accelerates to a constant speed of 80 km/h. Then a slow steering maneuver is executed until the vehicle lateral acceleration reaches 0.3 g and the reference steering wheel angle is recorded. Finally, a rapid (720 deg/sec) steering input is applied to the reference steering wheel angle. The test results are depicted in Fig 10. From Fig. 10(a)-(c), it is evident that the estimated longitudinal, lateral and vertical tire forces can also follow their true values with the normalized root mean square errors of 1.87%, 1.07% and 1.14%. Seen from Fig. 10(d), as opposed to the results under the hybrid maneuver, the longitudinal and lateral tire adhesion usage is mainly in Zones III and IV. The LTR evolution during the maneuver is depicted in Fig. 10(e) and the comprehensive vehicle stability state can be derived as shown in Fig. 10(f). Because of the emergency acceleration in the first stage, significant wheel slip occurs and the stability jumps from State I to State IV. During the second stage, the test vehicle experiences a low stability risk, and the lateral acceleration is less than 0.3 g so that the vehicle stability state remains in State I. In this state, the AFS system can work on its own to enhance vehicle handling performance. In the third stage, the test vehicle exhibits great yaw and rollover instability propensity due to the increased steering angle rate and high vehicle velocity. Tire slip also occurs in the third stage. It can be ascribed to the lateral load transfer, which results in a reduction of the inner-wheel vertical force. The vehicle stability prediction results with a prediction horizon of 50 time steps are delineated in Fig. 10(g). It can be seen that the comprehensive vehicle stability system can also efficiently predict the imminent vehicle instability risks in advance.

D. Comparison Analysis With State-of-The-Art Method

Ref. [31] presented a new delayed interconnected cascade-observer structure to reconstruct the forces acting on each tire in all directions. A 3-D vehicle model with four independent suspensions without considering the unsprung mass is developed to estimate the vertical tire force. As a tradeoff between accuracy and simplicity, the 2-D vehicle dynamics model and the Dugoff tire model are employed to describe longitudinal and lateral

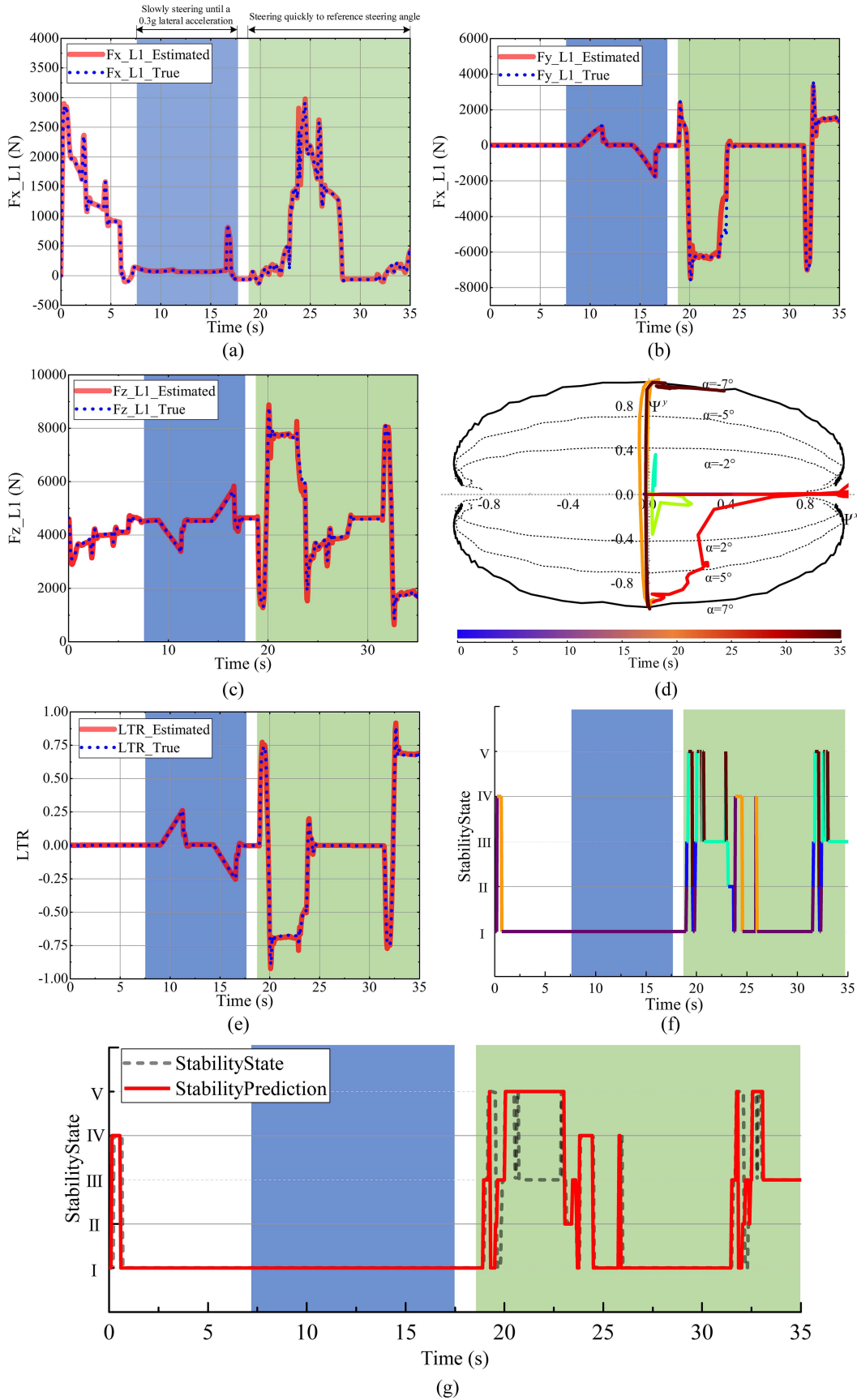


Fig. 10. The experimental results of the proposed comprehensive vehicle stability assessment system under the fish hook procedure: (a) is the estimated longitudinal tire force; (b) is the estimated lateral tire force; (c) is the estimated vertical tire force; (d) is the longitudinal and lateral adhesion usage; (e) is estimated LTR value; (f) is comprehensive vehicle stability state; (g) is the predicted vehicle stability state.

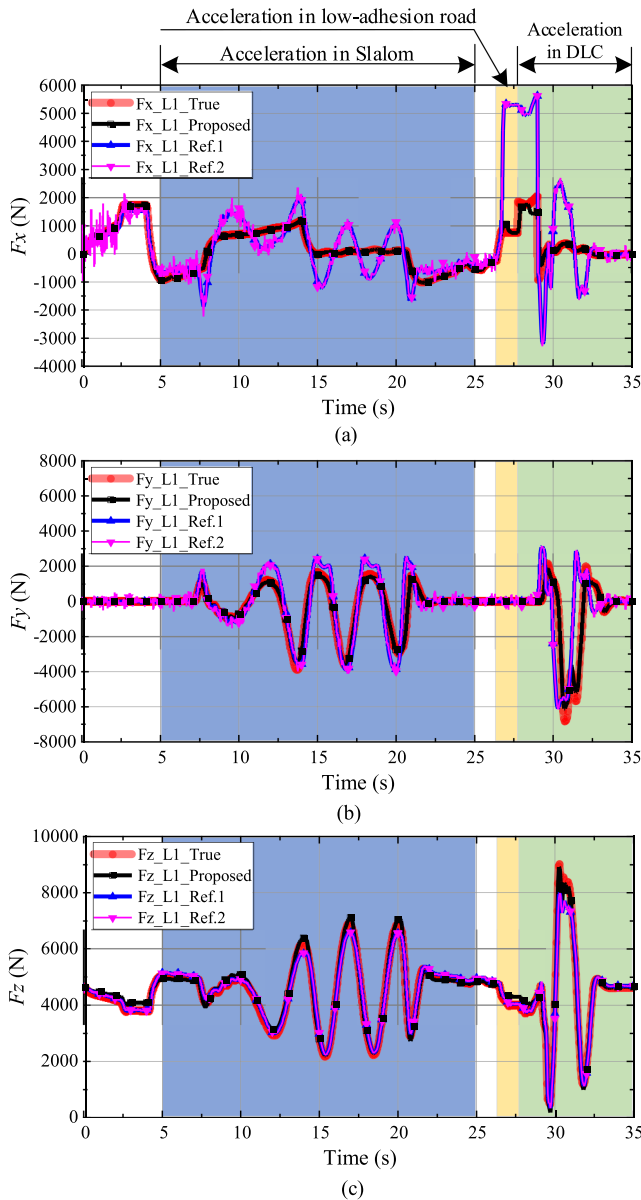


Fig. 11. The comparative HIL verification results of the proposed- and state-of-the-art tire force estimator under the hybrid maneuvers: (a) is the estimated longitudinal tire force; (b) is the estimated lateral tire force; (c) is the estimated vertical tire force.

tire dynamics, where the tire sideslip angle and slip ratio are taken as the inputs. Since both the longitudinal and lateral tire forces exhibit strong nonlinearities, a UKF observer is utilized to estimate tire forces. To make the comparison more convincing, artificial noises have also been added into the longitudinal velocity and vehicle sideslip angle based on Ref. [31], which further compromises the tire slip ratio and tire sideslip angle measurements. It is worth noted that the magnitudes of noise are set the same for the Oxford RT3100, which is a typical experimental device for vehicle state measurement. The HIL test results under the hybrid maneuver and fish hook procedure are shown in Fig. 11 and Fig. 12, respectively.

The subscript ref.1 represents the tire force estimation method proposed in Ref. [31], and subscript ref.2 is imposed by an

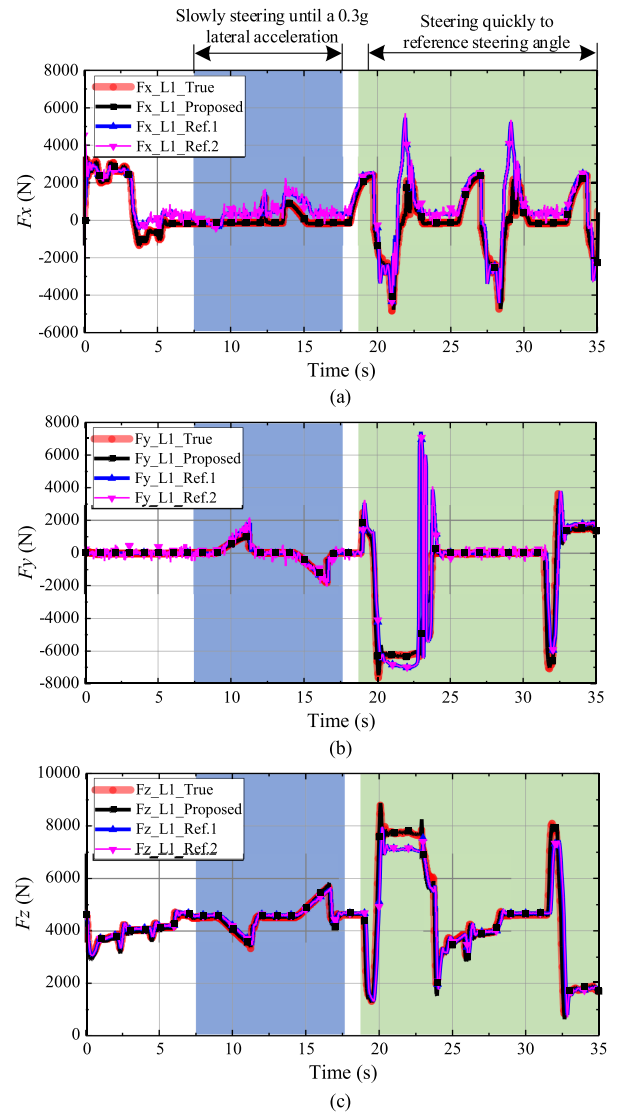


Fig. 12. The comparative HIL verification results of the proposed- and state-of-the-art tire force estimator under the fish hook procedure: (a) is the estimated longitudinal tire force; (b) is the estimated lateral tire force; (c) is the estimated vertical tire force.

appropriate noise based on ref.1. From Fig. 11(a), it can be seen that the proposed force estimator can accurately track the true value, while $F_{x_L1_ref.1}$ exhibits drastic fluctuation under the slalom maneuver. This can be ascribed to the tire slip ratio fluctuation, which is calculated based on the longitudinal velocity at the CG. In fact, the longitudinal velocity for tire slip ratio calculation needs to utilize a projection at the wheel corner instead of at the CG. Compared to $F_{x_L1_ref.1}$, there are some burrs on $F_{x_L1_ref.2}$ because of the existence of slip ratio noise. In the DLC maneuver, $F_{x_L1_ref.1}$ deviates from the true value due to the sharply increased slip ratio and the saturated longitudinal tire force. Fig. 11(b) shows the results of the lateral tire force estimation. Throughout the entire maneuver, $F_{y_L1_ref.1}$ can track the true value, but there is still a deviation at the peak point. The true lateral tire force does not increase with the increasing tire sideslip angle when the tire force is

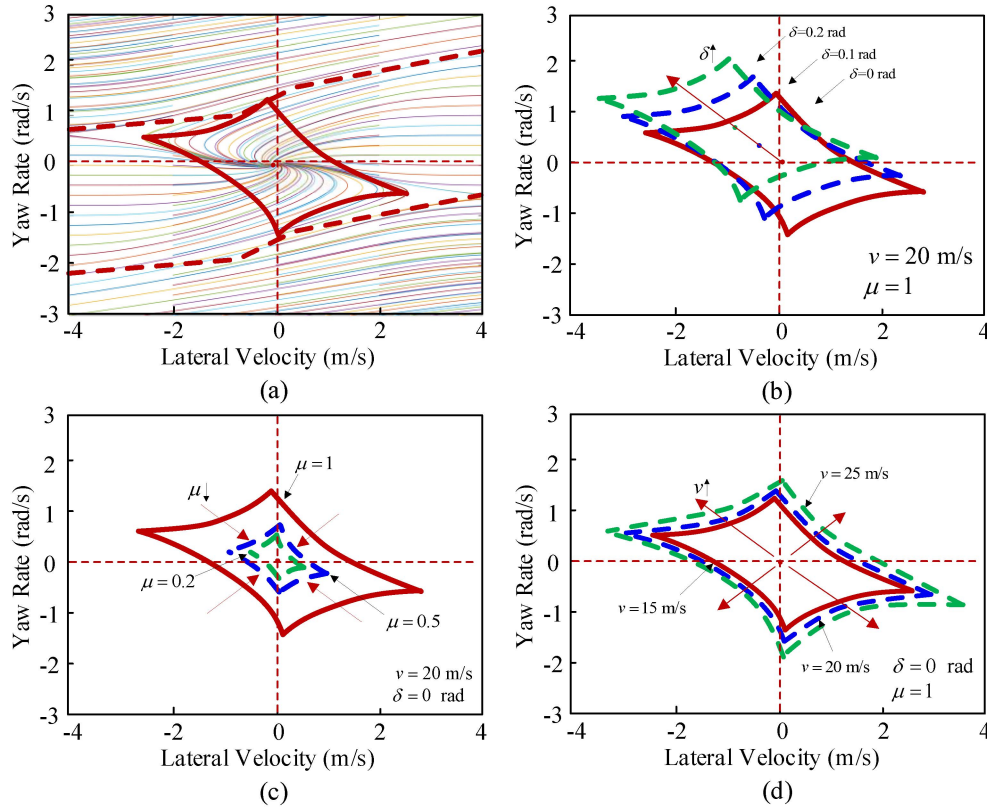


Fig. 13. The variation of yaw stability region along with different steering angle, speed and road adhesion.

saturated; but it is difficult for the Dugoff model to accurately capture the tire dynamics. From Fig. 11(c), it can be discerned that the vertical tire forces under the proposed estimator, ref.1 and ref.2 can follow the true vertical tire force. This is because they are all based on the independent suspension model. The minute deviation at the peak value for ref.1 can be ascribed to the neglect of the unsprung mass. Without using any tire model, the proposed tire force estimator is superior in both accuracy and robustness.

Fig. 12 shows the comparison results of tire force estimation during the fish hook procedure. Seen from Fig. 12(a), the proposed longitudinal tire force estimator can accurately track the true value while ref.1 and ref.2 see large deviations in the nonlinear region. Similarly, Fig. 12(b) shows that the lateral tire forces under ref.1 and ref.2 still exhibit large deviations in the nonlinear region. The vertical force estimation results are shown in Fig. 12(c). There are still small deviations between the true values and the ref.1 and ref.2 estimates due to the influence of the unsprung mass and the wheel alignment parameters.

A comprehensive vehicle stability assessment system that can simultaneously evaluate vehicle longitudinal, yaw and roll stability is still absent in the literature. In order to highlight the advantages of the proposed comprehensive stability assessment system, three vehicle stability assessment methods in the existing literature are selected for comparison. The tire slip ratio is selected for vehicle longitudinal stability evaluation; the $v_y - \omega_z$ phase plane is established for vehicle yaw stability assessment; and the LTR value is employed for vehicle roll stability assessment. The longitudinal and rollover stability

indicators are simple to understand. That is, a tire slip ratio greater than 0.2 is considered as longitudinal instability, while the absolute value of LTR greater than 0.7 is reckoned as rollover instability. For yaw stability, we select the state-of-the-art phrase plane method [12] for comparison, and obtain the yaw stability region under different steering angles, vehicle velocities and road adhesion coefficients through a large number of simulation tests. Fig. 13 depicts the variation of the yaw stability region along with different steering angles, vehicle velocities and road adhesion coefficients. We can evaluate the vehicle yaw stability by determining whether the lateral velocity and yaw rate are located within the stability region.

The vehicle stability assessment results of the proposed longitudinal-based, yaw-based and roll-based methods are shown in Fig. 14. For simplicity, we define the instability states of the yaw-based, longitudinal-based and roll-based methods as State III, IV and V, respectively. Seen from Fig. 14(a), the proposed comprehensive vehicle stability assessment system can match well with the longitudinal-based and the rollover-based stability evaluation method in terms of longitudinal and roll stability. For yaw stability, the proposed method can determine whether the vehicle is in the transition (13 s to 21 s) or the saturation zone, while the $v_y - \omega_z$ phase plane method can only evaluate vehicle yaw stability.

Fig. 14(b) shows the comparison results of vehicle stability evaluation in the fish hook procedure. It can be seen that the proposed scheme can also closely track the longitudinal-based and rollover-based methods throughout the test, and the yaw-based method can only determine the yaw instability. In contrast,

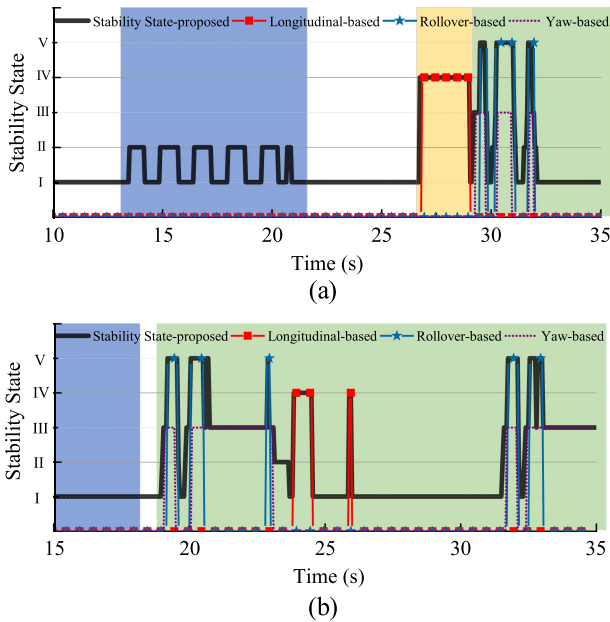


Fig. 14. The comparative HIL verification results of the proposed- and state-of-the-art vehicle stability assessment system: (a) is the results under under hybrid maneuvers; (b) is the results under under the fish hook procedure.

the proposed vehicle stability assessment system can not only judge vehicle yaw stability, but also classify stability levels for chassis coordinated control.

V. CONCLUSION

In this paper, an enabling vehicle stability assessment system is proposed based on tire forces estimation. First, the longitudinal, lateral and vertical tire forces are respectively estimated using the strong tracking unscented Kalman filter and the conventional Kalman filter based on low-cost on-board sensors. Then, a comprehensive vehicle longitudinal, yaw and roll stability space is established by utilizing the normalized tire friction ellipse and the Load Transfer Ratio value. Finally, the vehicle stability is determined and predicted based on the current driver's inputs. The hardware-in-loop experimental results show that the proposed vehicle stability assessment system can accurately estimate the longitudinal, lateral and vertical tire forces with the normalized root mean square errors of 1.87%, 1.07% and 1.43%, respectively, and exhibits satisfying performance for vehicle longitudinal, yaw and roll stability evaluation and prediction.

REFERENCES

- [1] X. Ding, Z. Wang, and L. Zhang, "Event-triggered vehicle sideslip angle estimation based on low-cost sensors," *IEEE Trans. Ind. Inform.*, vol. 18, no. 7, pp. 4466–4476, Jul. 2022.
- [2] L. Zhang, Z. Zhang, Z. Wang, J. Deng, and D.G. Dorrell, "Chassis coordinated control for full x-by-wire vehicles—a review," *Chin. J. Mech. Eng.*, vol. 34, no. 1, pp. 1–25, 2021.
- [3] H. Termous, H. Shraim, R. Talj, C. Francis, and A. Charara, "Coordinated control strategies for active steering, differential braking and active suspension for vehicle stability, handling and safety improvement," *Veh. Syst. Dyn.*, vol. 57, no. 10, pp. 1494–1529, 2018.
- [4] D. Yin, N. Sun, and J. S. Hu, "A wheel slip control approach integrated with electronic stability control for decentralized drive electric vehicles," *IEEE Trans. Ind. Inform.*, vol. 15, no. 4, pp. 2244–2252, Apr. 2019.

- [5] B. Peng, H. Zhang, F. Xuan, and W. Xiao, "Torque distribution strategy of electric vehicle with in-wheel motors based on the identification of driving intention," *Automot. Innov.*, vol. 1, no. 2, pp. 140–146, 2018.
- [6] R. de Castro, R. E. Araujo, and D. Freitas, "Wheel slip control of EVs based on sliding mode technique with conditional integrators," *IEEE Trans. Ind. Electron.*, vol. 60, no. 8, pp. 3256–3271, Aug. 2013.
- [7] J. Deur, D. Pavković, G. Burgio, and D. Hrovat, "A model-based traction control strategy non-reliant on wheel slip information," *Veh. Syst. Dyn.*, vol. 49, no. 8, pp. 1245–1265, 2011.
- [8] A. T. van Zanten, R. Erhardt, and G. Pfaff, "VDC, The vehicle dynamics control system of bosch," *SAE Trans.*, vol. 104, pp. 1419–1436, 1995.
- [9] C. G. Bobier-Tiu, C. E. Beal, J. C. Kegelmann, R. Y. Hindiyeh, and J. C. Gerdes, "Vehicle control synthesis using phase portraits of planar dynamics," *Veh. Syst. Dyn.*, vol. 57, no. 9, pp. 1318–1337, 2019.
- [10] S. M. Erlien, S. Fujita, and J. C. Gerdes, "Shared steering control using safe envelopes for obstacle avoidance and vehicle stability," *IEEE Trans. Intell. Transp. Syst.*, vol. 17, no. 2, pp. 441–451, Feb. 2016.
- [11] H. B. Pacejka, "Non-linearities in road vehicle dynamics," *Veh. Syst. Dyn.*, vol. 15, no. 5, pp. 237–254, 1986.
- [12] Y. Huang, W. Liang, and Y. Chen, "Stability regions of vehicle lateral dynamics: Estimation and analysis," *J. Dyn. Syst. Meas. Control.*, vol. 143, no. 5, 2021, Art. no. 051002.
- [13] J. Funke, M. Brown, S. M. Erlien, and J. C. Gerdes, "Collision avoidance and stabilization for autonomous vehicles in emergency scenarios," *IEEE Trans. Control Syst. Technol.*, vol. 25, no. 4, pp. 1204–1216, Jul. 2017.
- [14] C. Taeyoung and Y. Kyongsu, "Design and evaluation of side slip angle-based vehicle stability control scheme on a virtual test track," *IEEE Trans. Control Syst. Technol.*, vol. 14, no. 2, pp. 224–234, Mar. 2006.
- [15] C. E. Beal and C. Boyd, "Coupled lateral-longitudinal vehicle dynamics and control design with three-dimensional state portraits," *Veh. Syst. Dyn.*, vol. 57, no. 2, pp. 286–313, 2019.
- [16] G. Phanomchoeng and R. Rajamani, "New rollover index for the detection of tripped and untripped rollovers," *IEEE Trans. Ind. Electron.*, vol. 60, no. 10, pp. 4726–4736, Oct. 2013.
- [17] C. Wang, Z. Wang, L. Zhang, D. Cao, and D. G. Dorrell, "A vehicle rollover evaluation system based on enabling state and parameter estimation," *IEEE Trans. Ind. Inform.*, vol. 17, no. 6, pp. 4003–4013, Jun. 2021.
- [18] D. Chu, Z. Li, J. Wang, C. Wu, and Z. Hu, "Rollover speed prediction on curves for heavy vehicles using mobile smartphone," *IEEE Trans. Veh. Technol.*, vol. 130, pp. 404–411, Jul. 2018.
- [19] A. G. Nalecz, Z. Lu, and K. L. d'Entremont, "An investigation into dynamic measures of vehicle rollover propensity," SAE Tech. Paper 930831, 1993.
- [20] M. Ataei, A. Khajepour, and S. Jeon, "Model predictive control for integrated lateral stability, traction/braking control, and rollover prevention of electric vehicles," *Veh. Syst. Dyn.*, vol. 58, no. 1, pp. 1–25, 2019.
- [21] S. B. Choi, "Practical vehicle rollover avoidance control using energy method," *Veh. Syst. Dyn.*, vol. 46, no. 4, pp. 323–337, 2008.
- [22] S. Lapapong, A. A. Brown, K. S. Swanson, and S. N. Brennan, "Zero-moment point determination of worst-case manoeuvres leading to vehicle wheel lift," *Veh. Syst. Dyn.*, vol. 50, no. suppl, pp. 191–214, 2012.
- [23] C. Larish, D. Piyabongkarn, V. Tsourapas, and R. Rajamani, "A new predictive lateral load transfer ratio for rollover prevention systems," *IEEE Trans. Veh. Technol.*, vol. 62, no. 7, pp. 2928–2936, Sep. 2013.
- [24] H. B. Pacejka, "Tire and Vehicle Dynamics," Elsevier, 2012.
- [25] T. Hsiao, "Robust estimation and control of tire traction forces," *IEEE Trans. Veh. Technol.*, vol. 62, no. 3, pp. 1378–1383, Mar. 2013.
- [26] G. Erdogan, L. Alexander, and R. Rajamani, "Estimation of tire-road friction coefficient using a novel wireless piezoelectric tire sensor," *IEEE Sens. J.*, vol. 11, no. 2, pp. 267–279, Feb. 2011.
- [27] A. K. Madhusudhanan, M. Corno, and E. Holweg, "Vehicle sideslip estimator using load sensing bearings," *Control Eng. Pract.*, vol. 54, pp. 46–57, 2016.
- [28] S. Khaleghian, A. Emami, and S. Taheri, "A technical survey on tire-road friction estimation," *Friction*, vol. 5, no. 2, pp. 123–146, 2017.
- [29] L. R. Ray, "Nonlinear tire force estimation and road friction identification: Simulation and experiments," *Automatica*, vol. 33, no. 10, pp. 1819–1833, 1997.
- [30] M. Doumiati, A. Victorino, A. Charara, and D. Lechner, "Onboard real-time estimation of vehicle lateral tire-road forces and sideslip angle," *IEEE/ASME Trans. Mechatron.*, vol. 16, no. 4, pp. 601–614, Aug. 2011.
- [31] R. A. Cordeiro, A. C. Victorino, J. R. Azinheira, P. A. V. Ferreira, E. C. de Paiva, and S. S. Bueno, "Estimation of vertical, lateral, and longitudinal tire forces in four-wheel vehicles using a delayed interconnected cascade-observer structure," *IEEE/ASME Trans. Mechatron.*, vol. 24, no. 2, pp. 561–571, Apr. 2019.

- [32] J. A. Cabrera, J. J. Castillo, J. Pérez, J. Velasco, A. Guerra, and P. Hernández, "A procedure for determining tire-road friction characteristics using a modification of the magic formula based on experimental results," *Sensors*, vol. 18, no. 3, pp. 896–912, Mar. 2018.
- [33] A. Rezaeian et al., "Novel tire force estimation strategy for real-time implementation on vehicle applications," *IEEE Trans. Veh. Technol.*, vol. 64, no. 6, pp. 2231–2241, 2014.
- [34] X. Ding, Z. Wang, L. Zhang, and C. Wang, "Longitudinal vehicle speed estimation for four-wheel-independently-actuated electric vehicles based on multi-sensor fusion," *IEEE Trans. Veh. Technol.*, vol. 69, no. 11, pp. 12797–12806, 2020.
- [35] J. Wong, *Theory of Ground Vehicles*. New York, NY, USA: Wiley, 1976.
- [36] D. H. Zhou and P. M. Frank, "Strong tracking filtering of nonlinear time-varying stochastic systems with coloured noise: Application to parameter estimation and empirical robustness analysis," *Int. J. Control*, vol. 65, no. 2, pp. 295–307, 1996.
- [37] Q. Xia, M. Rao, Y. Ying, and X. Shen, "Adaptive fading kalman filter with an application," *Automatica*, vol. 30, no. 8, pp. 1333–1339, Aug. 1994.
- [38] D.-J. Jwo and S.-Y. Lai, "Navigation integration using the fuzzy strong tracking unscented kalman filter," *J. Navig.*, vol. 62, no. 2, pp. 303–322, Apr. 2009.
- [39] A. Sorniotti and N. D'Alfio, "Vehicle dynamics simulation to develop an active roll control system," SAE Tech. Paper 2007-01-0828, 2007.
- [40] X. Ding, Z. Wang, and L. Zhang, "Event-triggered vehicle sideslip angle estimation based on low-cost sensors," *IEEE Trans. Ind. Inform.*, vol. 18, no. 7, pp. 4466–4476, Jul. 2022, doi: [10.1109/TII.2021.3118683](https://doi.org/10.1109/TII.2021.3118683).
- [41] M. Blundell and D. Harty, *The Multibody Systems Approach to Vehicle Dynamics*, 2nd ed., USA, NY, New York: Elsevier Science and Technology Books, 2015.



Xiaolin Ding received the B.S. degree in automotive engineering from the Hebei University of Technology, Tianjin, China, in 2016. He is currently working toward Ph.D. degree in mechanical engineering with the National Engineering Research Center for Electric Vehicles, Beijing Institute of Technology, Beijing, China.

His research interests include vehicle system dynamics and control of Full X-by-Wire Four-Wheel-Independently-Actuated Electric Vehicles



Zhenpo Wang (Member, IEEE) received the B. Eng. degree in mechanical design and manufacturing from Tongji University, Shanghai, China, in 2000, and the Ph.D. degree in automotive engineering from Beijing Institute of Technology, Beijing, China, in 2005. He is currently a Professor with the School of Mechanical Engineering, Beijing Institute of Technology, and also the Director of the National Engineering Research Center for Electric Vehicles. His research interests include Big-Data technology, battery safety management, wireless charging system, and advanced vehicle

chassis control for electric vehicles.

Prof. Wang is current the Executive Editor-in-Chief of the JOURNAL OF GREEN ENERGY AND INTELLIGENT TRANSPORTATION. He is also on the Editorial Board of CHINA JOURNAL OF HIGHWAY AND TRANSPORT.



Lei Zhang (Member, IEEE) received the Ph.D. degree in mechanical engineering from the Beijing Institute of Technology, Beijing, China, in 2016, and the Ph.D. degree in electrical engineering from the University of Technology, Sydney, NSW, Australia, in 2016. He is currently a Tenured Associate Professor with the School of Mechanical Engineering, Beijing Institute of Technology. His research interests include control theory and engineering applied to electrified vehicles, with focus on battery management techniques, vehicle dynamics control, and autonomous

driving technology.

He is the Section Editor-in-Chief with Sustainable Transportation for *Sustainability*. He is currently an Associate Editor for IEEE OPEN JOURNAL OF VEHICULAR TECHNOLOGY, *Frontiers in Energy Research*, *Proceedings of the Institution of Mechanical Engineers Part C-Journal of Mechanical Engineering Science*, *SAE International Journal of Electrified Vehicles*, and *SAE International Journal of Connected and Autonomous Vehicles*. He is also on the Editorial Boards of *Plos One*, *Electronics*, *China Journal of Highway and Transport* and *Green Energy and Intelligent Transportation*, and is an Academic Editor of *Automotive Innovation*.



Jizheng Liu received the B.S. degree in mechanical engineering from XUTELI School, Beijing Institute of Technology, China, in 2019. He is currently working toward the Ph.D. degree in mechanical engineering with the National Engineering Research Center for Electric Vehicles, Beijing Institute of Technology, Beijing, China.

His research interests mainly include vehicle dynamics, control of Four-Wheel-Independent-Actuated Electric Vehicles and vehicle platoon control under Vehicle-to-Everything communication.